# Azerbaijan Journal of Physics

# FİZİKA

1E

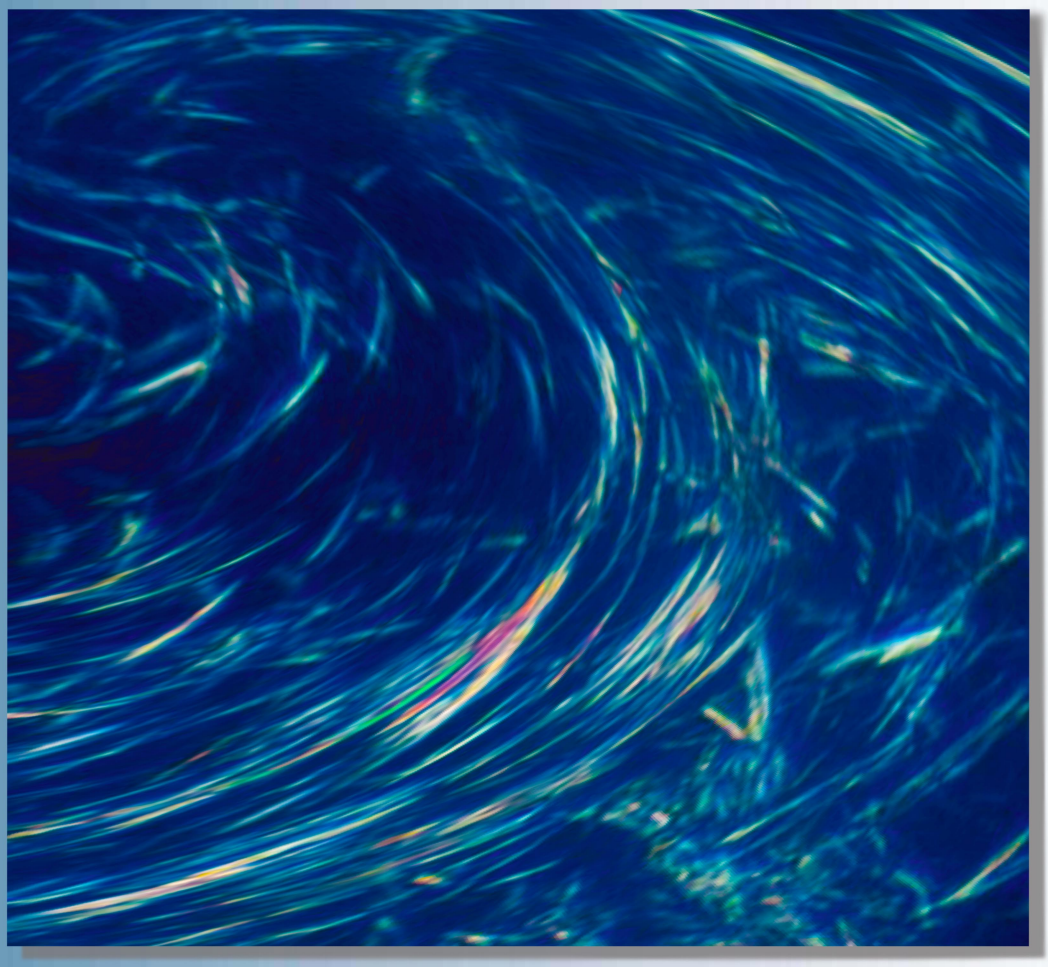

www.physics.gov.az

XXX

2024

Published from 1995
Ministry of Press and Information
of Azerbaijan Republic,
Registration number 514, 20.02.1995

**ISSN 1028-8546**
vol. XXX, Number 01, 2024
Section: E

# *Azerbaijan Journal of Physics*

# *FIZIKA*

*Ministry of Science and Education Republic of Azerbaijan*
*Institute of Physics*



**PUBLISHING OFFICE**

131, H. Javid ave., AZ-1143, Baku
Ministry of Science and Education Republic of Azerbaijan
Institute of Physics

Tel.: (99412) 539-51-63, 539-32-23
Fax: (99412) 537-22-92
E-mail: jophphysics@gmail.com
Internet: www.physics.gov.az

It is authorized for printing:

# PREPARATION OF $Y_{0,3}Cd_{0,7}Ba_2Cu_3O_{7-d}$, $Y_{0,1}Cd_{0,9}Ba_2Cu_3O_{7-d}$, $CdBa_2Cu_3O_6$ MATERIALS AND ANALYSIS OF THEIR SUPERCONDUCTING TRANSITIONS

**V.M. ALIEV[1], G.I. ISAKOV[1], J.A. RAGIMOV[2], V.I. EMINOVA[1], S.Z. DAMIROVA[1], G.A. ALIEVA[3]**

*[1]Institute of Physics Ministry of Science and Education of Azerbaijan, AZ 1143, Baku, G. Javid Ave., 131*

*[2]Azerbaijan Medical University, Baku, AZ 1022, st. Bakikhanova, 23*

*[3]Institute of National HP Ministry of Science and Education of Azerbaijan AZ 1025, Baku, Khojaly Ave., 30*

*E-mail: v_aliev@bk.ru*

A study was carried out of the possibility of the influence of substitution from 70% to 100% of yttrium by cadmium in $YBa_2Cu_3O_{7-\delta}$ polycrystals on the superconducting states of the synthesized materials. As a result, high-resistivity samples were obtained. In the normal phase they had semiconductor passages. Of the $Y_{0,3}Cd_{0,7}Ba_2Cu_3O_7$, $Y_{0,1}Cd_{0,9}Ba_2Cu_3O_7$ and $CdBa_2Cu_3O_7$ samples, only the $Y_{0,3}Cd_{0,7}Ba_2Cu_3O_{7-\delta}$ sample made a superconducting transition at 84K. For the sample $Y_{0,3}Cd_{0,7}Ba_2Cu_3O_{7-\delta}$ HTSC material, the critical temperature in the mean field approximation ($T_c^{mf}$), the 3D-2D crossover temperature ($T_0$), the coherence length of the Cooper pair were determined, the temperature $T_c$ of the SC transition and $T_G$-temperature were determined Ginsburg.

**Keywords:** superconductivity, coherence lengths, 3D-2D temperature Crossover.
**PACS:** 74.25. Fy, 74.20.Mn, 74.72. ± h, 74.25. ± q, 74.25.Jb

## 1. INTRODUCTION

The works [1-8] analyzed in detail the substitution of yttrium in the composition Y–Ba–Cu–O with rare earth elements (Nd, Tm, Sm, Gd, Er, Yb, La, Dy, Ho, etc.).

Note that Y–Ba–Cu–O, despite the maximum number of possible isomorphic substitutions [1–8], is not among the systems where isomorphic heterovalent substitution leads to an increase in the transition temperature Tc. Despite this, the study of substitution in the classical $YBa_2Cu_3O_{7-\delta}$ structure remains an urgent problem, since it allows us to draw certain conclusions about the mechanism of superconductivity and the contribution of Y, Ba, Cu layers to superconductivity.

However, the proximity of the ionic radius of yttrium and cadmium gave us the basis to conduct a study on the substitution of cadmium for yttrium in the Y–Ba–Cu–O composition. In this case, we believed that the difference in the ionic radii of Y and Cd leads to a distortion of the YBCO crystal structure. This leads to the formation of defects in the structure and the appearance of pinnings in the crystal structure. The formed pinnings reduce the probability of splitting of Cooper pairs and create the possibility of a HTSC material having a high resistance value in the normal phase transitioning to the superconducting state.

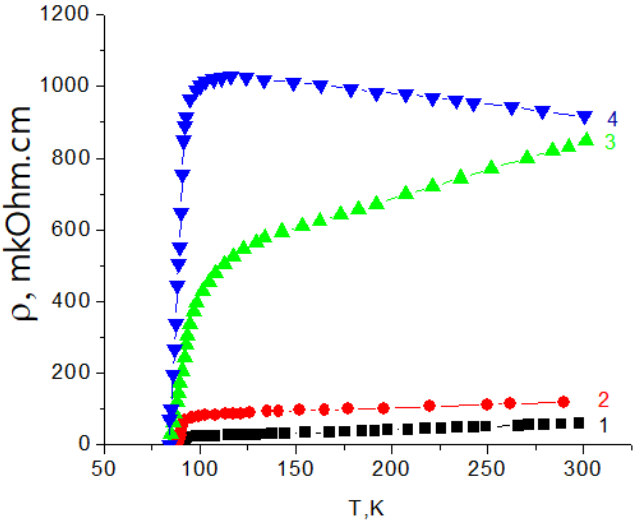


*Fig. 1.* Temperature dependences of resistivity ρ of samples: 1- $Y_{0,9}Cd_{0,1}Ba_2Cu_3O_{7-\delta}$ [9]; 2- $Y_{0,7}Cd_{0,3}Ba_2Cu_3O_{7-\delta}$ [9]; 3- $Y_{0,5}Cd_{0,5}Ba_2Cu_3O_{7-\delta}$ [10]; 4-$Y_{0,3}Cd_{0,7}Ba_2Cu_3O_{7-\delta}$ [11]

131, H.Javid ave, AZ-1143, Baku
Institute of Physics
E-mail: jophphysics@gmail.com

Note that so far the substitution of yttrium for cadmium from 0.1 to 0.7 parts in the $YBa_2Cu_3O_{7-\delta}$ HTSC material has been obtained and analyzed (Fig. 1) [9,10,11].

The result of the study from $Y_{0,1}Cd_{0,9}Ba_2Cu_3O_7$ and $CdBa_2Cu_3O_6$ is shown in Fig. 2.

Of the samples (Fig. 1 and 2) $Y_{0,3}Cd_{0,7}Ba_2Cu_3O_{7-\delta}$, $Y_{0,1}Cd_{0,9}Ba_2Cu_3O_{7-\delta}$ and $CdBa_2Cu_3O_6$, only the $Y_{0,3}Cd_{0,7}Ba_2Cu_3O_{7-\delta}$ sample made a superconducting transition at 84 K.

Analysis of Fig. 2 shows that both samples, $Y_{0,1}Cd_{0,9}Ba_2Cu_3O_{7-\delta}$ and $CdBa_2Cu_3O_6$ in the normal phase have a semiconductor behavior. Further lowering the temperature of the samples makes a metallic move and there is hope that, with a change in synthesis technology, it is possible to obtain the indicated samples.

In connection with the above, this work is devoted to the study of the normal state of $Y_{0,3}Cd_{0,7}Ba_2Cu_3O_{7-\delta}$ in the temperature range $T^*>T>T_c$ and the determination of its physical characteristics ($\rho$, $T_c$, $T_c^{mf}$, $T_0$, $T_G$ and $\xi_c(0)$).

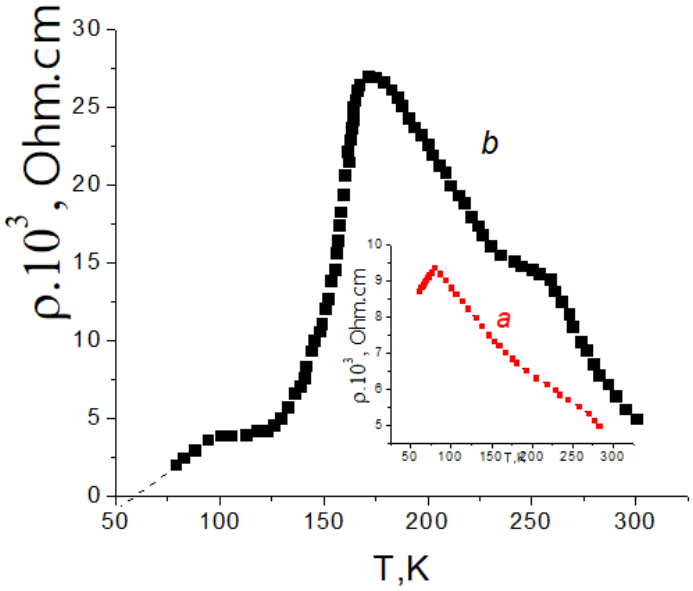


*Fig.2.* Temperature dependences of resistivity ρ of samples: *a*-$Y_{0,1}Cd_{0,9}Ba_2Cu_3O$ and $CdBa_2Cu_3O_6$.

Of the samples (Fig.1 and 2) $Y_{0,3}Cd_{0,7}Ba_2Cu_3O_{7-\delta}$, $Y_{0,1}Cd_{0,9}Ba_2Cu_3O_{7-\delta}$ and $CdBa_2Cu_3O_6$, only the $Y_{0,3}Cd_{0,7}Ba_2Cu_3O_{7-\delta}$ sample made a superconducting transition at 84 K.

Analysis of Fig. 2 shows that both samples, $Y_{0,1}Cd_{0,9}Ba_2Cu_3O_{7-\delta}$ and $CdBa_2Cu_3O_6$ in the normal phase have a semiconductor behavior. Further lowering the temperature of the samples makes a metallic move and there is hope that, with a change in synthesis technology, it is possible to obtain the indicated samples.

In connection with the above, this work is devoted to the study of the normal state of $Y_{0,3}Cd_{0,7}Ba_2Cu_3O_{7-\delta}$ in the temperature range $T^*>T>T_c$ and the determination of its physical characteristics ($\rho$, $T_c$, $T_c^{mf}$, $T_0$, $T_G$ and $\xi_c(0)$).

## 2. EXPERIMENT

The synthesis and sample preparation for measurements of the polycrystalline compound $Y_{0,3}Cd_{0,7}Ba_2Cu_3O_{7-\delta}$, $Y_{0,1}Cd_{0,9}Ba_2Cu_3O_{7-\delta}$ and $CdBa_2Cu_3O_6$ is identical to [9,10]. The synthesis was carried out in two stages. At the first stage, the initial components in a stoichiometric ratio were mixed and annealed in an air environment at a temperature of 1120 K for 25 hours. At the second stage, the resulting compositions were annealed in an oxygen environment (P = 1.2–1.5 atm) at a temperature of 1190 K for 25 hours and slowly cooled to room temperature. It has been established that when up to 90% of yttrium is replaced by cadmium in the $YBa_2Cu_3O_{7-\delta}$ composition, the superconducting transition is not preserved (Fig. 2). The electrical resistance of the samples was measured using a standard four-probe scheme.

We believe that the superconducting transition of the $Y_{0,3}Cd_{0,7}Ba_2Cu_3O_{7-\delta}$ sample occurs as a result of the difference in the ionic radius of Y and Cd leading to distortion of the YBCO crystal structure. This leads to the formation of defects in the structure and the appearance of pinnings in the crystal structure. The formed pinnings reduce the probability of splitting of Cooper pairs and create the possibility of a HTSC material having a high resistance value in the normal phase transitioning to the superconducting state.

In order to study the composition of the resulting $Y_{0,3}Cd_{0,7}Ba_2Cu_3O_{7-\delta}$ HTSC material, it was subjected to X-ray diffraction analysis. The result of the study is presented in Fig. 3.

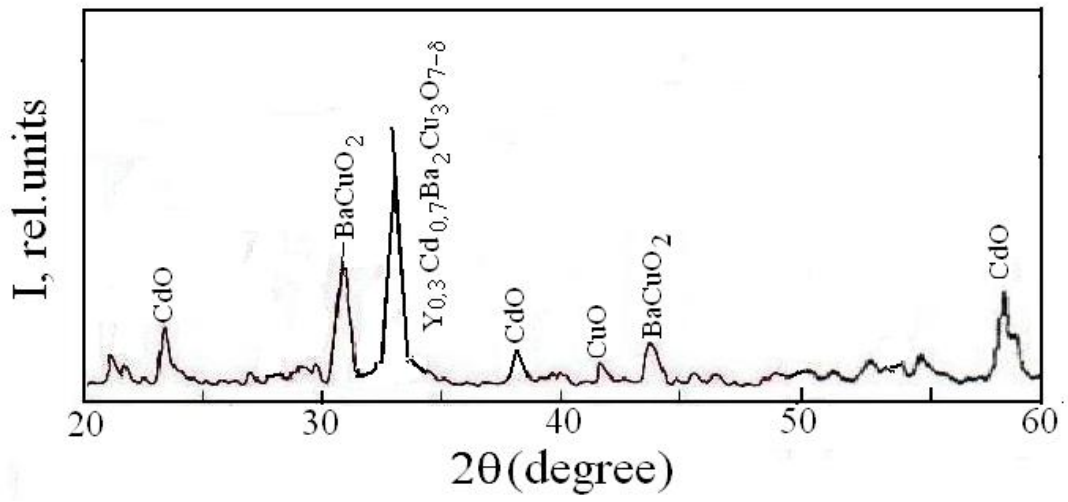


*Fig.3.* X-ray diffraction pattern of sample $Y_{0,3}Cd_{0,7}Ba_2Cu_3O_{7-\delta}$

X-ray diffraction analysis showed that in addition to the main material $Y_{0,3}Cd_{0,7}Ba_2Cu_3O_{7-\delta}$, there are also oxides $BaCuO_2$ and CdO in the X-ray. However, we note that in various compositions of SP polycrystals there are always, in addition to the main crystalline granules, various oxides.

## 3. RESULTS AND DISCUSSION

The temperature dependence of the resistivity $\rho(T)=\rho ab\ (T)$ of the synthesized $Y_{0,3}Cd_{0,7}Ba_2Cu_3O_{7-\delta}$ polycrystal is given in Fig. 4.

Figure 4 shows the temperature dependences of the resistivity $\rho(T)=\rho ab\ (T)$ of the studied $Y_{0,3}Cd_{0,7}Ba_2Cu_3O_{7-\delta}$ polycrystal.

The course of the temperature dependence of the resistivity of the $Y_{0,3}Cd_{0,7}Ba_2Cu_3O_{7-\delta}$ sample in the normal phase is well extrapolated by the expression $\rho_n(T)= (\rho_0+ kT +BT^2$ (here B and k are some constants ρ0=1077 μOhm.cm, B=-0.0005 and k=-0.35). The straight lines represent the $\rho_n(T)$ dependences extrapolated to the low temperature region.

This linear dependence of the $Y_{0,3}Cd_{0,7}Ba_2Cu_3O_{7-\delta}$ sample, extrapolated to the low temperature region, was used to determine the excess conductivity $\Delta\sigma(T)$ according to [12]:

$$\Delta\sigma(T) = \rho^{-1}(T) - \rho_n^{-1}(T). \quad (1)$$

From Fig. 4 it can be seen that the value of the critical temperature of the sample when doped with Cd in the case considered remains close to ~ 85K, while the resistivity ρ(T) of the $Y_{0,3}Cd_{0,7}Ba_2Cu_3O_{7-\delta}$ ample in the normal phase at 300K is ρ(300K)=918.3 μOhm• cm.

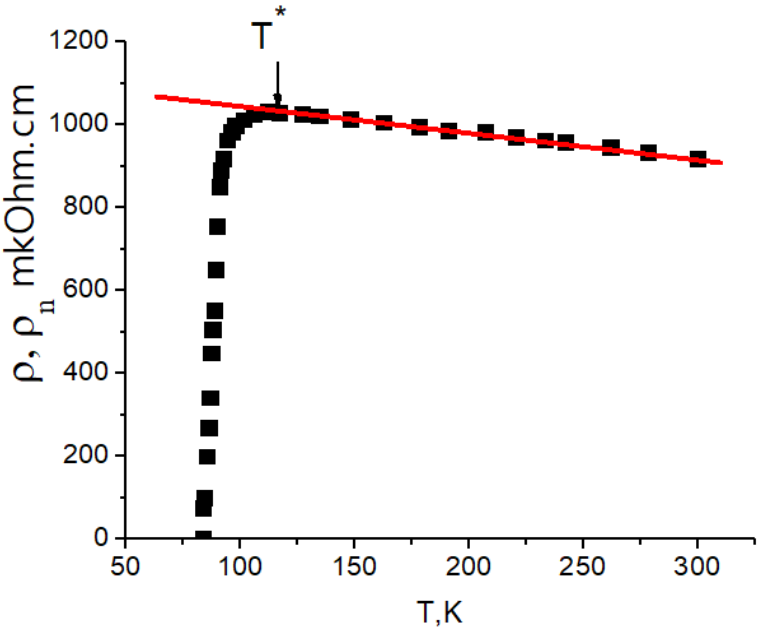


*Fig.4.* Temperature dependences of the resistivity ρ of the sample $Y_{0,3}Cd_{0,7}Ba_2Cu_3O_{7-\delta}$

In order to determine the FLP within the framework of the local pair (LP) model [6], it is first necessary to determine the critical temperature in the mean field approximation, which separates the FLP region from the region of critical fluctuations [6, 13]. Fluctuation of the SP order parameter $\Delta_0$ directly near $T_c$ (where $\Delta_0 < K_BT$), where it is not taken into account in the Ginzburg–Landau theory [1314]. Determination of Tcmf is necessary for the analysis of the FLP and PSH, which is used in equation (2) to calculate the reduced temperature:

$$\varepsilon=(T/T_c^{mf} - 1) \quad (2)$$

The method for determining Tcmf for the $Y_{0.3}Cd_{0.7}Ba_2Cu_3O_{7-\delta}$ sample based on analysis of the temperature dependence is presented in Fig. 5.

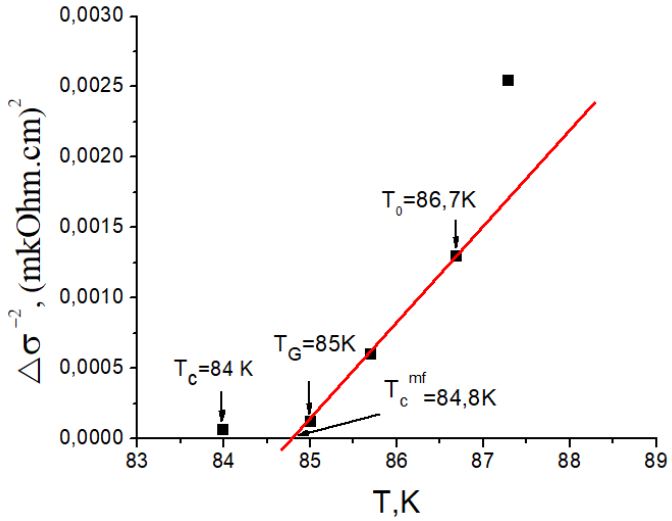


*Fig. 5.* Temperature dependence of the inverse square of the excess conductivity $\sigma^{-2}$ (T) of the $Y_{0,3}Cd_{0,7}Ba_2Cu_3O_{7-\delta}$ polycrystal, which determines the Tcmf of the sample. Arrows the characteristic temperatures $T_c$, $T_G$ and $T_0$ are indicated.

From Fig. 5, the temperature $T_c$ of the SC transition is determined, $T_G$ is the Ginzburg temperature, up to which the mean field theory is valid as temperatures decrease [15, 16], and T0 is the 3D–2D crossover temperature, limiting the region of 3D–AL fluctuations from above [17, 18].

Having determined Tcmf (Fig. 5), it is possible to plot the dependence of ln σ on ln ε for the $Y_{0,3}Cd_{0,7}Ba_2Cu_3O_{7-\delta}$ sample (Fig. 6).

From Fig. 6 it is clear that, near $T_c$, the FLP is well approximated by the fluctuation contribution of AL for 3D systems (3) (straight 3D–AL lines with slope $\lambda = -1/2$). This means that classical 3D FLP is always realized in cuprate HTSCs when T tends to Tc and $\xi c(T) > d$ [6, 19, 20, 21]. Above $T_0$, the dependence of ln ε sharply changes its slope. This dependence with a slope of $\lambda = -1$ is characteristic of 2D–AL fluctuations [22]. Having determined the values of ε (Fig. 6), the values of the coherence length along the c axis (ξc) were calculated using the equation $\xi c(0) = d\sqrt{(\varepsilon)}0$. Note that in HTSC near $T_c$ the coherence length along the c axis is greater than the corresponding size of the YBCO unit cell d = c = 11.7 Å [9] and fluctuation Cooper pairs (FCPs) interact throughout the entire volume of the superconductor. The calculated value of the coherence length of $Y_{0,3}Cd_{0,7}Ba_2Cu_3O_{7-\delta}$ HTSC material is 1.74 Å.

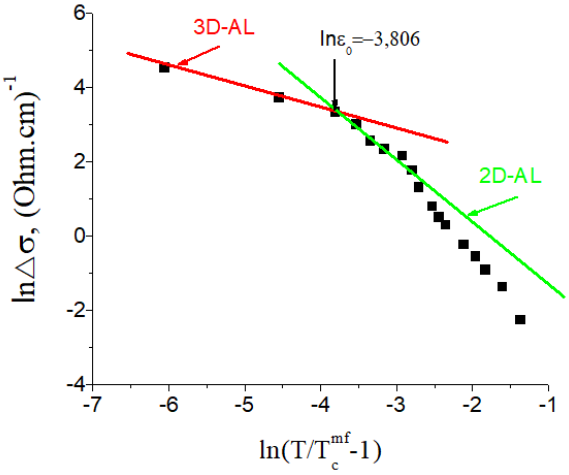


*Fig.6.* Dependence of the logarithm of excess conductivity on ln(T/Tc-1) of the sample $Y_{0,3}Cd_{0,7}Ba_2Cu_3O_{7-\delta}$. Solid lines - calculation within the framework of theory Aslamazov -Larkin.

## 4. CONCLUSION

Thus, we can come to the conclusion that in the $Y_{0,3}Cd_{0,7}Ba_2Cu_3O_{7-\delta}$ we studied, the formation of local pairs of charge carriers at $T>>T_c$ is possible [21, 22].

The study showed that near $T_c$ the fluctuation conductivity is well described within the framework of the Aslamazov–Larkin fluctuation theory: 3D–AL. Above the 3D–2D crossover temperature, the 2D–AL theory is applicable.


[1] *T. Suzuki, T. Yamazaki, and R. Sekine.* J. Mat. Sci. Lett. 8, 381 1989.

[2] *V.N. Narozhnyi and V.N. Kochetkov.* Phys. Rev. B53, 5856, 1996.

[3] *M. Murakami, N. Sakai, and T. Higuchi.* Supercond. Sci.Technol. 12, 1015, 1996.

[4] *A.L. Soloviev, V.M. Dmitriev.* FNT 33, 32 2007. [LowTemp. Phys. 33, 23, 2007].

[5] *R.V. Vovk, M.A. Obolensky, A.A. Zavgorodniy, A.V. Bondarenko, M.G. Revyakin.* FNT, 33, 546, 2007.

[6] *L.P. Kozeev, M.Yu. Kamenev, A.I. Romanenko, O.B. Anikeeva, V.E. Fedorov*. Materials 6th International Conference “Crystals: growth, properties, real structure, application": Alexandrov, September 8–12, 2003, VNIISIMS Publishing House.

[7] *E.V. Yakubovich, N.N. Oleynikov, V.A. Ketsko, I.V. Arkhangelsky.* Dokl. RAS 386, 502, 2002.

[8] *S. Kambe, G. Samukama, K. Yamaguchi, O. Ishu, I. Shime, T. Nomura, S.Ohshima, K.Okuyama, T. Itoh, H. Suematsu, and H. Yamauchi.* Solid State Phys. 108, 283 (1998)

[9] *V.M. Aliev, R.I. Selim-zade, J.A. Ragimov, L.V. Omelchenko, E.V. Petrenko.* FNT, vol. 46, №9, p. 1068–1077, 2020.

[10] *V. M. Aliev, G.I. Isakov, J.A. Ragimov, R.I.Selim-zade, G.A.Alieva.* Solid State Physics bodies, 65, no. 3, p. 404-410, 2023.

[11] *V.M. Aliyev, G.I. Isakov, J.A. Rahimov, V.I. Eminova, S.Z. Damirova, G.A. Aliyeva.* AJP FIZIKA, vol. X1X, №1, 44-41, 2023.

[12] *A.L. Soloviev, V.M. Dmitriev.* FNT, vol. 35, №3, pp. 227-264, 2009.

[13] *P.G. De Gennes.* Superconductivity of Metals and Alloys, W. A. Benjamin, INC., NewYork–Amsterdam, p. 280. 1966.

[14] *L.G. Aslamazov and A. I. Larkin.* Phys. Lett. A 26, 238 (1968).

[15] *A. Kapitulnik, M. R. Beasley, C. Castellani, and C. Di Castro.* Phys. Rev. B 37, 537 (1988).

[16] *S. Hikami and A. I. Larkin.* Mod. Phys. Lett. B 2, 693 (1988)

[17] *Y.B. Xie*. Phys. Rev. B 46, 13997 (1992).

[18] *A.L. Solovyov, L.V.Omelchenko, R.V.Vovk, S.N. Kamchatnaya.* FNT 43, 1050, 2017.

[19] *A.L. Solovjov, L.V. Omelchenko,*

[20] *V.B. Stepanov, R.V. Vovk, H.-U. Habermeier, H. Lochmajer, P. Przyslupski, and K. Rogacki.* Phys. Rev. B 94, 224505 (2016).

[21] *W. Lang, G. Heine, W. Kula, and Roman Sobolewski. Phys. Rev. B* 51, 9180 (1995).

[22] *В.В. Флоренть*ев, *А.В. Инющкин, А.И.Талденков и др.,* СФХТ, 3, 10, 2 (1990)

[23] *Ya. Ponomarev, M. Mikheev, M. Sudakova, S. Tchesnokov, and S. Kuzmichev,* Phys. Status Solidi C, 6, 2072 (2009).


*Received: 17.01.2024*

# EFFECT OF ANNEALING ON THE THERMOELECTRIC PROPERTIES OF EXTRUDED BULK NANOSTRUCTURED SAMPLES OF THE $Bi_{0,85}Sb_{0,15}$ SOLID SOLUTION

**M.M. TAGIYEV[1.2], G.D. ABDINOVA[2], I.A. ABDULLAEVA[3], X.F. ALIEVA[2], T.I. PIRIEVA[2], A.A. JABIYEVA[1], K.N. ALIYEVA[4]**

*[1]Azerbaijan State Economic University,Baku city, Istiglaliyat str.,6. AZ-1001, Baku, Azerbaijan.*

*[2]Institute of Physics named after G.B. Abdullaev Ministry of Science and Education. AZ-1143, H. Javid ave.,131, Baku, Azerbaijan.*

*[3]Institute of Radiation Problems of the Ministry of Science and Education. AZ 1143, B. Vahabzade Ave., 9, Baku, Azerbaijan.*

*[4]Azerbaijan Food Safety Institute. Suleyman Sani Akhundov 73C, Baku, Azerbaijan. AZ-1124.*

*e-mail: mail_tagiyev@mail.ru*

Extruded bulk nanostructured samples of the $Bi_{0,85}Sb_{0,15}$ solid solution were obtained from particles with an average size of ~$2\cdot10^5$; 950; 650; 380; 30 and 15 nm and their thermoelectric properties were investigated in the range of ~77-300K. The samples that had not undergone heat treatment and the same samples that had undergone heat treatment were examined. It was found that the electrical and thermal properties of the $Bi_{0,85}Sb_{0,15}$ solid solution samples significantly depend on the size of nanoparticles and post-extrusion heat treatment. Heat treatment leads to a decrease in the concentration of current carriers, an increase in the mobility of current carriers and the overall thermal conductivity of the studied samples, which is mainly due to the electronic component of thermal conductivity.

**Keywords:** extrusion, annealing, solid solution, nanoparticle, texture.
**PACS**: 72.15 Eb, 7350 It

## 1. INTRODUCTION

Solid solutions of Bi-Sb systems, especially high-strength extruded materials based on these systems, are the most effective materials for creating various low-temperature thermo- and magneto-thermoelectric energy converters [1-4]. The extrusion method has high productivity and gives wide possibilities to analyze thermoelement branches [5,6]. However, there is almost no work on studying the patterns of influence of particle sizes (especially in the nanosize region) on the transport parameters of these materials. With a decrease in particle size, boundary effects begin to known themselves in the transport properties, including the processes of scattering of phonons and electrons at particle boundaries [7,8]. Nanostructuring of thermoelectrics allows the use of a new controllable parameter - the size of nanostructural elements - as an additional factor influencing the figure of merit, which can lead to an increase in the thermoelectric figure of merit in bulk nanocrystalline thermoelectric materials [9].

It was found that post-extrusion annealing leads to a decrease in the dislocation density and defect concentration in the samples of Bi-Sb systems [10]. Therefore, the study of galvanomagnetic properties in extruded nanostructured samples with different particle sizes, annealed and not annealed in a wide range of temperatures and magnetic field strengths, is of certain scientific and practical interest.

Taking into account the above, in order to study the influence of annealing and nanoscale effects on the electrical and thermal properties of bulk nanostructured samples of the $Bi_{0,85}Sb_{0,15}$ solid solution, in this work extruded bulk nanostructured samples, $Bi_{0,85}Sb_{0,15}$ materials, were obtained and their transport properties were studied in the range ~77÷300K.

## 2. EXPERIMENTAL PART

The synthesis of the $Bi_{0,85}Sb_{0,15}$ composition was carried out by direct alloying of the components in the appropriate stoichiometry in a quartz ampoule removed to a residual pressure of ~$10^{-2}$ Pa. Bismuth of the "Vi-000" grade and antimony of the "Su-0000" grade were used as the starting components.

Nano-sized $Bi_{0,85}Sb_{0,15}$ particles were obtained using an AGO-2 ball mill. The particle size in the powder was changed by changing the time of crushing the source material in the mill. The average particle sizes in the powder were determined on an XRD D8 ADVANCE X-ray installation, Bruker, Germany based on diffraction spectra using the Scherrer formula [11] and using the TORAS-4.2 and EVA program, the crystallite sizes were specified to be ~$2\cdot10^5$; 950; 650; 380; 30 and 15 nm.

$Bi_{0,85}Sb_{0,15}$ solid solution powders were pressed at room temperature and pressure ~3.5 T/cm$^2$ into briquettes with a diameter of ~30 mm, which is convenient for extrusion. Extrusion was carried out on an MS-1000 hydraulic press from a diameter of 30 mm to a diameter of 6 mm using special equipment. Technological parameters of the extrusion process (temperature, pressure, drag velocity, etc.) were chosen such that the formation of extruded rods took

131, H.Javid ave, AZ-1143, Baku
Institute of Physics
E-mail: jophphysics@gmail.com

place under conditions of super plasticity without macro- and micro-disturbances.

Samples for research were cut out from various extruded rods using an A207.40M electric spark installation in the form of rectangular parallelepipeds with dimensions of 3 x 5 x 12 mm. The damaged layer formed on the surface of the samples during cutting was removed by electrochemical etching in a solution of $KOH+C_4H_4O_6+H_2O$. Annealing of the samples was carried out in quartz ampoules evacuated to a pressure of ~$10^{-1}$ Pa at a temperature of ~503 K for 2 hours.

Electrical conductivity ($\sigma$), thermo-electromotive force ($\alpha$), Hall ($R_H$) and thermal conductivity ($\chi$) coefficients of samples that were not annealed and the same samples that were annealed after extrusion were studied in the range ~77-300K and magnetic field strength (H ) up to ~$74x10^4$ A/m. Electrical and thermal parameters were measured by the method described in [12] along the length of the sample, i.e. in the direction of extrusion. The measurements used a cryostat with a design that allows one to measure $\sigma$, $\alpha$, $R_H$ and $\chi$ in one sample installation. Electrical conductivity and Hall coefficient were measured at direct current. Probes were pre-soldered onto the sample to remove the voltage drop that occurs when measuring $\sigma$, $R_H$ and thermo-electromotive force when measuring the coefficient $\alpha$. The temperature gradient created along the sample during measurements of $\alpha$ and $\chi$ was determined using two copper-constantan thermocouples, one of whose heads was soldered to the sample.

To eliminate the electrical asymmetry of the probes, measurements of the voltage drop across the probes when determining $\sigma$ were carried out in two opposite directions of current through the sample. To eliminate the influence of asymmetry of Hall contacts and other parasitic electromotive forces caused by galvanomagnetic and thermomagnetic effects, $R_H$ measurements were carried out in two opposite directions of current and magnetic field. In this case, by rotating the cryostat in a magnetic field, the maximum value of the Hall voltage on the sample was achieved. Electrical conductivity and galvanomagnetic effects were measured under isothermal conditions and thermopower under adiabatic conditions. The execution of these conditions was controlled by measurements of the thermo- electromotive force of the sample and directly with thermocouples soldered to the sample.

Thermal conductivity measurements were carried out using an absolute stationary method along the sample. Due to the fact that solid solutions based on bismuth-antimony have low thermal conductivity, heat loss due to radiation from the heating furnace and crystal, as well as heat carried away by the wires of the heating furnace and wires for receiving various signals, are significant.

The measurements took into account the heat carried away by the above wires, as well as the heat carried away by radiation from the surface of the sample and the electric heater.

During the measurements, a vacuum of ~$10^{-3}$ Pa was created and maintained inside the cryostat, where the sample was located.

Voltage values, electromotive force and current strength during measurements were determined using a digital voltmeter and ammeter brand B7-21 and SM3D.

The geometric dimensions of the samples and the distances between the probes were determined by an MBS-1 microscope with an accuracy class of 0.005 mm.

An electromagnet was used to provide a magnetic field for intensity measurements up to 1.0 Tesla.

The error in measuring electrical parameters and thermal conductivity was ~3-5%.

## 3. RESULTS AND ITS DISCUSSION

The obtained measurement results are presented in Figures 1, 2, 3.

From Fig. 1 it can be seen that in samples that have undergone heat treatment and have not undergone heat treatment, the dependences of the coefficients $\sigma$ and $\alpha$ on the particle size at ~77 K are non-monotonic. Heat treatment leads to an increase in $\sigma$ and a decrease in $\alpha$ in all studied samples, except for the sample with particle sizes ~$2\cdot10^5$ nm.

With heat treatment, the coefficient of total thermal conductivity ($\chi$) increases for all samples, except for the sample with 15 nm nanoparticles. Using the expressions $\chi_L = \chi - \chi_e$ and $\chi_e = L\sigma T$, the electronic ($\chi_e$) and lattice ($\chi_L$) components of thermal conductivity were calculated. Here $L = A(k/e)^2$ Lorentz number, k is Boltzmann's constant, e is the electron charge. The value of A was estimated from the dependence of A on the thermo-electromotive force coefficient [13].

At low temperatures, with a decrease in particle size in extruded samples, an increase in $\chi$ and a decrease in the phonon part of thermal conductivity ($\chi_L$) are observed, as well as an increase in $\sigma$ and a decrease in $\alpha$ and $R_H$. This is due to a decrease in the size of the crystals and an increase in the concentration of boundaries, which leads to an increase in the electron concentration and a decrease in the scattering of phonons and electrons in the samples. As particle sizes increase, particle disorientation weakens due to thermal energy during hot extrusion (~470K). Therefore, with increasing particle sizes, the degree of texture of the samples increases. At the same time, the perfection of the particles also increases, which leads to an increase in the mobility of current carriers $\mu$ and a slight decrease in their concentration n.

From the values of $R_H$ and $\sigma$ at ~77K, the Hall mobility $\mu = R_H \sigma$ of current carriers was calculated. It was found that with an increase in the size of nanoparticles during heat treatment, the value of m as a function of $\mu \sim T^{-m}$ increases from 1.42 ÷1.57 for samples without heat treatment, to 1,81÷2,6 for the same samples that undergone heat treatment. The increase in $R_H$ and $\mu$ at ~77K after heat treatment is apparently associated mainly with a change in the concentration of defects and the parameter A, which characterizes the scattering mechanism in the expression $R_H = A/en$, except for the sample with particle sizes ~$2\cdot10^5$ nm, where e - electron charge.

During the extrusion of nanostructured samples of the $Bi_{0,85}Sb_{0,15}$ solid solution, due to plastic deformation, most of the polycrystal particles are

oriented so that their trigonal axis becomes parallel to the extrusion axis, i.e. texture is formed. During plastic deformation, various crystal lattice defects simultaneously appear in individual particles. The degree of texture in nanostructured samples will depend on the technological parameters of the extrusion process, the size of particles (nanoparticles) and post-extrusion heat treatment. During heat treatment, disorientation of particles may also occur due to thermal energy, i.e. change in the degree of texture of the extruded sample [14].

The most considerable change in the degree of texture during annealing occurs in nanostructured samples with the smallest particle sizes. With increasing particle sizes in bulk nanostructured samples, the effect of heat treatment on the degree of texture is weakened. Defects associated with boundaries between crystallites (particles) lead to the fact that samples with minimal particle sizes (~ 15 nm) have a high concentration of current carriers among the studied samples. The experimental results show that a decrease in the size of nanoparticles leads to a decrease in mobility due to electron scattering at the boundaries of nanoparticles. Therefore, the degree of texture during extrusion, recrystallization and disorientation of particles during heat treatment, as well as electrical and thermal parameters will depend on the size of the particles in the sample.

From Fig. 2 it can be seen that as the particle size decreases, the magnetoresistance of the samples decreases. For all samples with heat treatment, the value of magnetoresistance increases significantly.

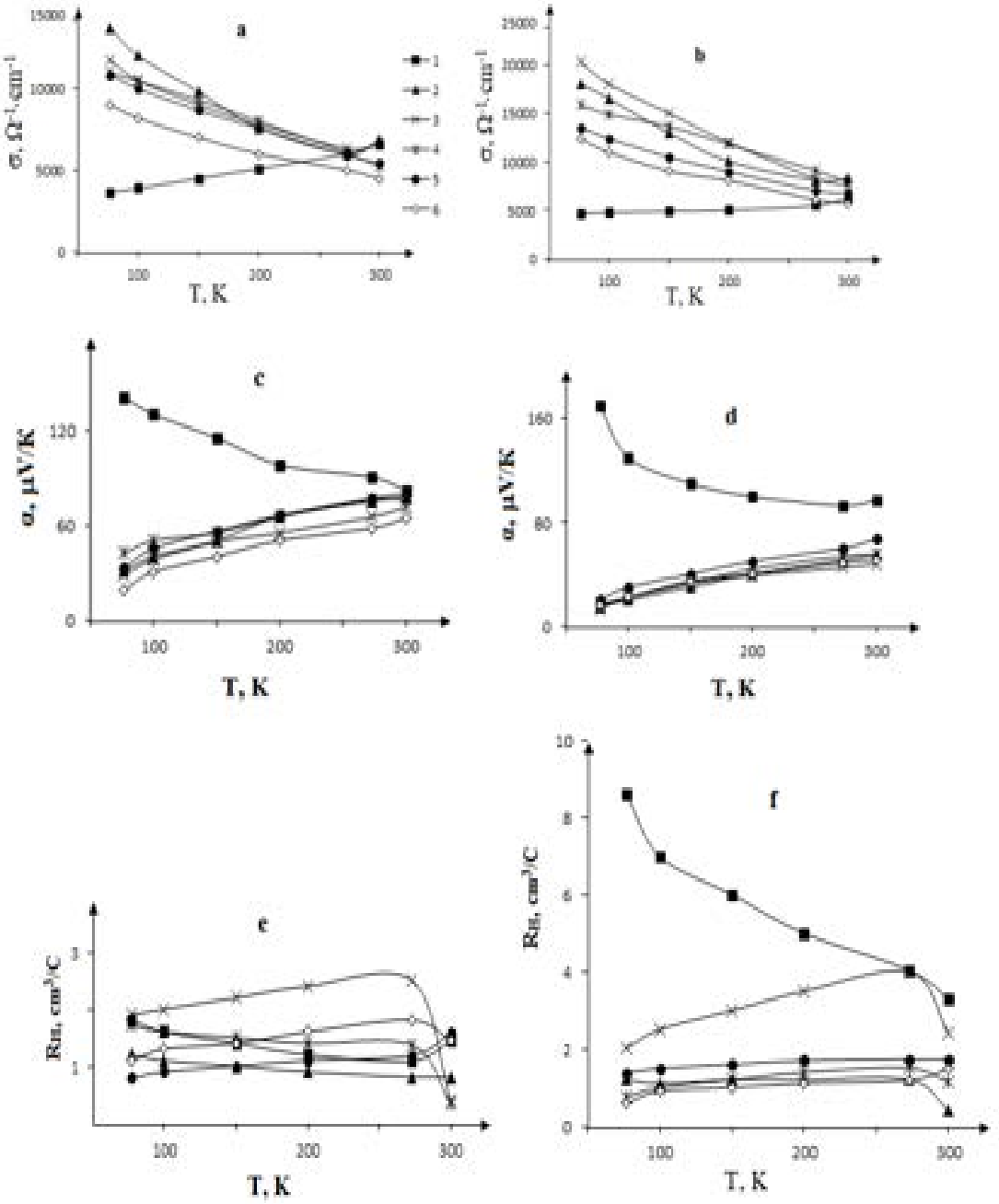

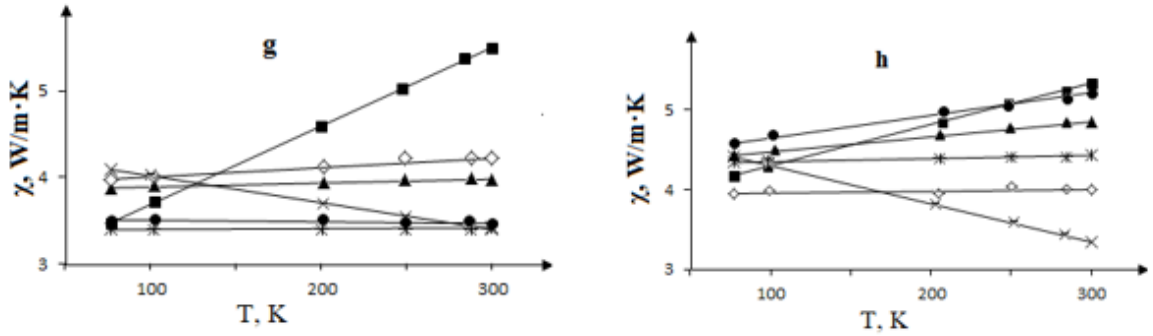


*Fig. 1.* Temperature dependences of the coefficients of electrical conductivity (σ), thermo-emf (α), Hall ($R_H$) and thermal conductivity (χ) of extruded samples of the $Bi_{0,85}Sb_{0,15}$ solid solution with different particle sizes that have not undergone heat treatment (a,c,e,g) and have undergone heat treatment (b,d,f,h). Curves 1-6 refer to samples with particle sizes - $2 \cdot 10^5$; 950; 650; 380; 30 and 15 nm, respectively.

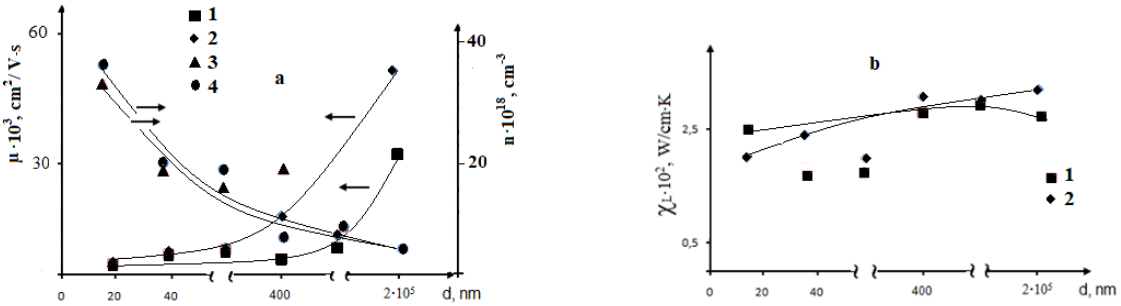


*Fig. 2.* Dependences of the concentration (n), mobility (μ) of current carriers (a) and the phonon part of thermal conductivity ($\chi_L$) (b) of nanostructured extruded samples of the $Bi_{0,85}Sb_{0,15}$ solid solution on the particle size at ~77 K. Fig. a, curves 1,3 - unannealed samples, 2,4 - annealed samples, Fig. b- 1- annealed samples, 2- unannealed samples.

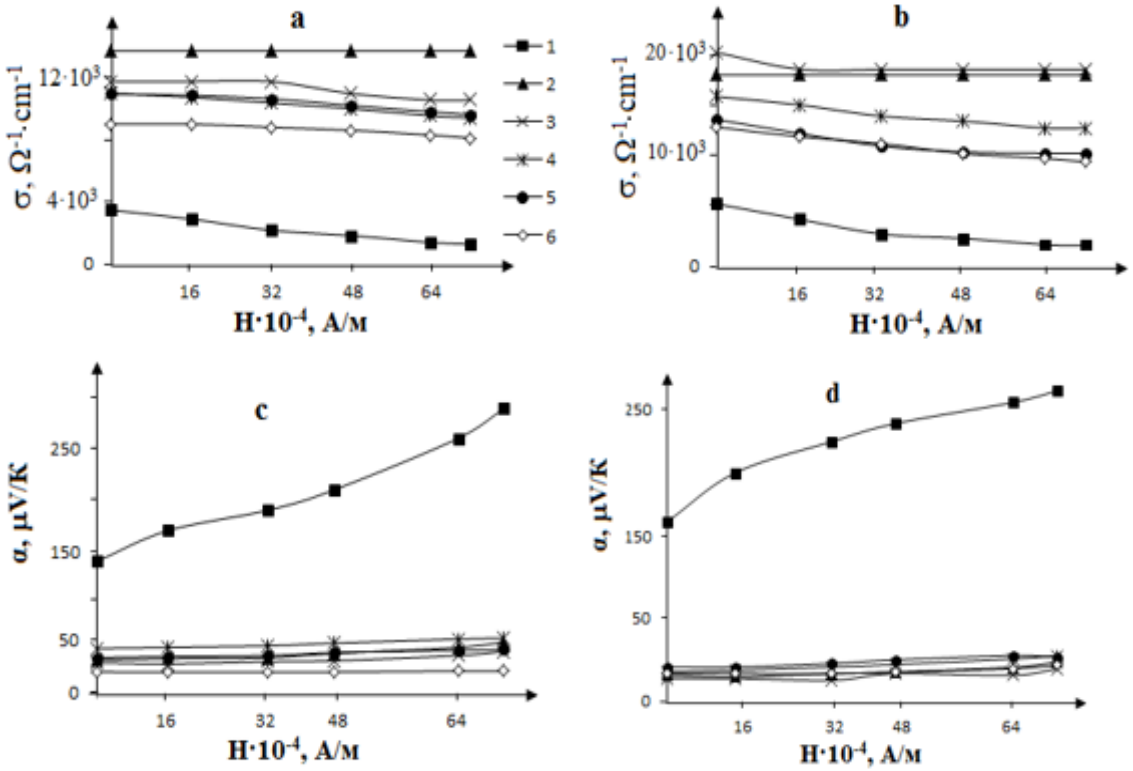

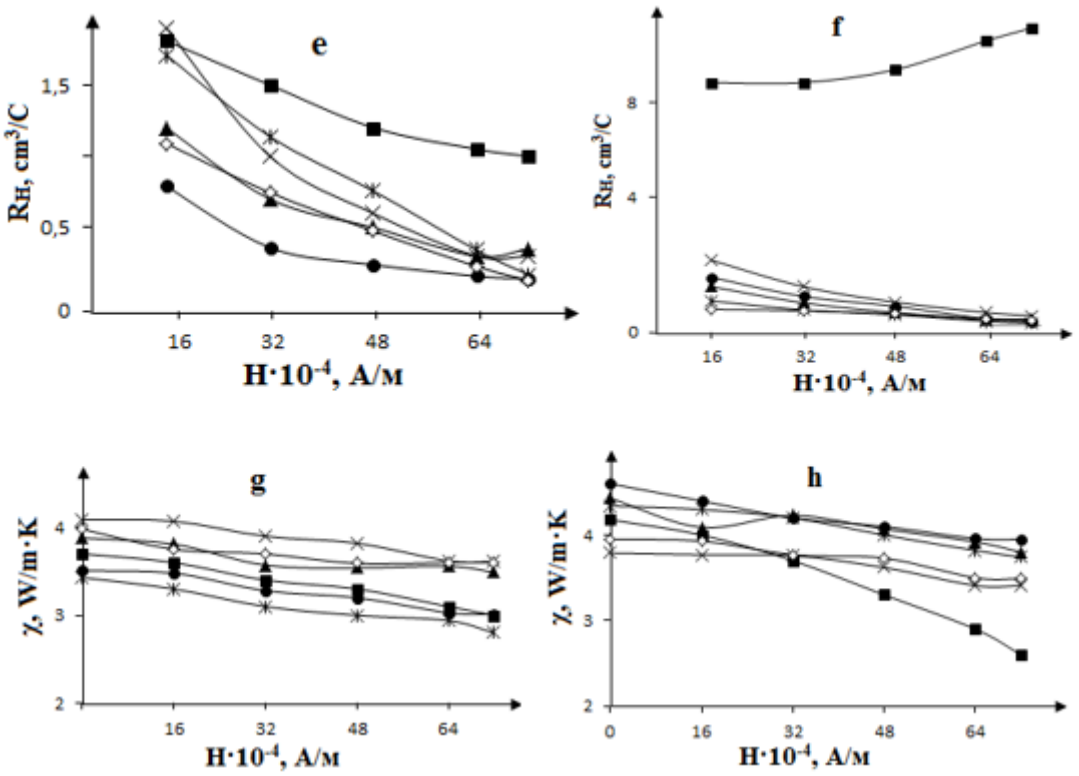


*Fig. 3.* Dependences of electrical conductivity ($\sigma$), thermo-e.m.f. ($\alpha$),Hall ($R_H$) and thermal conductivity ($\chi$) coefficients of the extruded samples of $Bi_{0,85}Sb_{0,15}$ solid solution with various sizes of particles before (a, c, e, g ) and after (b, d, f, h ) heat treatment on magnetic fields intensity at ~77 K. The designations are the same as in Fig.1

At ~77K, the dependences of α on the magnetic field strength for the studied samples with and without heat treatment are identical and almost independent of H, except for the sample with particle sizes ~$2\cdot10^5$ nm (Fig. 2).

In a magnetic field, some redistribution of the roles of various carriers in the total current in the sample occurs. The contribution of weakly scattering current carriers to the total current decreases due to an increase in the resistance to their movement, which, with a constant total current, leads to an increase in the contribution of strongly scattering particles. In this case, the average energy of current carriers changes. During heat treatment, scattering by acoustic phonons begins to prevail in samples, to which fast charge carriers are more susceptible than slow ones. Therefore, in a magnetic field, the total current of fast carriers increases and, consequently, the average energy of current carriers increases. Therefore, the dependence of α on the magnetic field in samples with heat treatment is stronger than in samples that have not undergone heat treatment.

In the scattering of phonons in samples at low temperatures (~77 K), the dominant role is played by texture, and electrons are mainly scattered by structural defects. As the size of grains (nanoparticles) increases, the concentration of structural defects formed during plastic deformation decreases, which leads to a decrease in the electron concentration n, $\chi_e$, an increase in μ, and a slight increase in $\chi_L$.

During heat treatment, partial destruction of the texture and “healing” of structural defects occurs [13], which leads to a decrease in n and an increase in μ, σ and $\chi_L$.

The nature of the dependence of electrical and thermal parameters on the magnetic field strength for both unannealed and annealed samples remains the same at ~300K. However, at ~300K the influence of heat treatment and magnetic field on the kinetic parameters is greatly weakened.

## 4. CONCLUSION

Thus, the dependences of the electrical and thermal parameters of bulk nanostructured extruded samples of the $Bi_{0,85}Sb_{0,15}$ solid solution on grain sizes and heat treatment show that the dominant role in the scattering of current carriers and phonons in samples at ~77K is played by particle sizes, defects associated with boundaries between particles, and the degree of ordering ( texture) of particles during extrusion, recrystallization and disorientation of crystallites during heat treatment. Heat treatment leads to a decrease in n and an increase in μ, $\chi$, $\chi_e$ and magnetoresistance. With an increase in particle size,

due to an increase in the energy required for particle orientation, the degree of texture in samples during deformation decreases, which leads to a weakening of the dependence of $\chi_p$ on particle size. The change in thermal parameters is satisfactorily explained by the changes occurring in the structure of the samples during extrusion and heat treatment which correlates with the changes occurring in the electrical parameters during these processes.


[1] *N.P. Stepanov.* Electron–plasmon interaction in bismuth with an acceptor dopant. Russian Physics Journal. 2004. V.47. №3. P. 262-272.

[2] *M.M. Tagiyev.* Influence of grain sizes and lead impurities on thermoelectric properties of extruded samples of $Bi_{0.85}Sb_{0.15}$ solid solution. Inorganic Mater. 2021. V.57 (7). P. 113-118.

[3] *M.M. Tagiyev.* Electrical anisotropy in extruded specimens of $Bi_{0.85}Sb_{0.15}$ solid solution. Russian Physics Journal. 2018. V. 60 №10. P. 1794-1797.

[4] *N.A. Sidorenko, Z.M. Dashevsky.* Effective Bi-Sb crystals for thermoelectric cooling at temperatures T ≤ 180 K. FTP. 2019.V. 53. Issue. 5. P.693-697.

[5] *L.D. Ivanova, L.D. Petrova, V.Yu. Granatkina, V.S. Zemskov, et.al.* Extruded materials for thermoelectriccoolers. Inorganic Mater. 2009. V.45. №2. P.123-128.

[6] *L.P. Bulat, l.V. Bochcov, I.A. Nefedova, R. Ahiska.* Nanostructuring as a way to increase the efficiency of thermoelectric. Scientific and Technical Journal of Information Technologies, Mechanics and Optics. 2014. V. 4 №92. P.48-56.

[7] *B.Sh. Barkhalov, M.M. Tagiyev, G.Z. Bagiyeva, G.D. Abdinova, et.al.* Effect of Grain Sizes on the Electrical and Thermal Conductivity of Extruded $Bi_{0.5}Sb_{1.5}Te_3$ Solid Solution Samples. Russian Physics Journal. 2019. V. 62. №4. P. 664-672.

[8] *V.A. Komarov, A.V. Suslov, M.V. Suslov.* Galvanomagnetic properties of $Bi_{85}Sb_{15}$ thin films on different substrates. Semiconductors. 2017. V. 51. № 6. P. 702-705.

[9] *L.P. Bulat, V.B. Osvencky, G.I. Pivovarov, A.A.Snarskii, E.V. Tatyanin, A.A.O. Tay.* The influence of phonon thermal conductivity on thermoelectric figure of merit of bulk nanostructured materials with tunneling contacts. Proc. VI Eur. Conf. on Thermoelectrics. 2008. P.12-14.

[10] *F.S. Samedov, M.M. Tagiyev, and D.Sh. Abdinov.* Effect of heat treatment on the properties of extruded Pb-doped $Bi_{0.85}Sb_{0.15}$ solid solutions. Inorganic Mater. 1998.V. 34. №7. P. 847-850.

[11] *D.M. Heiker, L.S. Zevin.* X-ray diffractometry, Moscow: Fizmatgiz 1963. 380. P.

[12] *A.S. Okhotin, A.S. Pushkarsky, R.P. Borovikova, V.A. Smirnov.* Methods for measuring the characteristics of thermoelectric materials and converters. M.: Science. 1974. 168. P.

[13] *I.A. Smirnov, V.I. Tamarchenko.* Electronic thermal conductivity in metals and semiconductors. L.: Science. 1977. 151. P.

[14] *Л.П. Булат, В.В. Овсенский, Д.А. Пшенай-Северин.* Влияние распределения зерен по размерам на решеточную теплопроводность наноструктурированных материалов на основе $Bi_2Te_3$-$Sb_2Te_3$. ФТТ. 2013. V.55. № 12. P. 2323 -2330.


*Received: 08.02.2024*

# MONOCHROMATIC WAVE PROPAGATION IN VACUUM

**E.R. HASANOV[1,2], Sh.G. KHALILOVA[2], R.K. MUSTAFAYEVA[1]**
*[1]Baku State Uviversity Acad. Z. Khalilov,str.23, Baku, Azerbaijan Republic*
*[2]Institute of Physics,MSE, AZ-1143, H. Javid 131, Baku, Azerbaijan Republic*
*shahlaganbarova@gmail.com*

Vacuum still remains a mysterious medium from a physical point of view, especially its physical properties. The passaging of a monochromatic wave is examined through a vacuum of size L in our work. A monochromatic wave has a certain energy, and when passing through a vacuum it should not lose energy. At different values of the vacuum size, according to the properties of the vacuum, there should be no loss of energy by the wave. If energy loss occurs as a wave passes through, the cause of the energy loss is inhomogeneity. The inhomogeneity of the vacuum proves the existence of some particles in the vacuum, i.e. vacuum is ordinary matter. We can say that a certain part of the energy of a monochromatic wave is absorbed by matter, i.e. vacuum. In this work, the energy of a monochromatic wave is calculated before and after passing through a vacuum of size L. It has been proven that the ratio of the energy of a monochromatic wave before passing through a vacuum is less than 1. This means that the monochromatic wave was scattered inelastically in a vacuum and vacuum is a dense medium. After the passage of the vacuum wave, the length of the monochromatic wave decreases. A monochromatic wave loses energy in a vacuum.

**Keywords:** vacuum, energy, inelastic interaction, monochromatic wave, absorption, inhomogeneity.
**PACS:** 78,55, 73.22.CD, 73.22

## INTRODUCTION

Quantum mechanics, as a mathematical method, is based on the wave function. In the one-dimensional case, the monochromatic wave function has the form

$$\psi(x,t) = ce^{i(kx-\omega t)} = ce^{i\left(kx-\frac{Et}{\hbar}\right)} \tag{1}$$

Here $k$ -wave vector

$k = \frac{2\pi}{\lambda}n, (n = 0,\pm1,\pm2,\ldots)$, $\lambda$ -wavelenth, $K$ - energy of wave in vacuum, which is related to the wave vector as follows

$$E = \frac{\hbar^2 k^2 n^2}{2m_0}, \quad n = 0,\pm1,\pm2,\ldots \tag{2}$$

$m_0$ - free electron mass

Wave function (1) satisfies Schrödinger equation

$$\frac{\partial\psi}{\partial t} = \frac{i\hbar}{2m_0}\frac{\partial^2\psi}{\partial x^2} \tag{3}$$

Let's pretend that a monochromatic wave falls on vacuum with energy

$$E_{before} = \frac{2\pi^2\hbar^2}{m_0\lambda_0^2} \tag{4}$$

## THEORY

In the view of classical physics, this wave should not change energy after leaving the vacuum with a length of $L$ However, we will show that the energy (4) changes after leaving the vacuum as $L$. This means that the vacuum interacts with a monochromatic wave. So, there is interaction with the wave in vacuum. Using the Schrödinger equation (3), we calculate the energy in vacuum

From (1) we calculate $\frac{\partial\psi}{\partial t}$ and $\frac{\partial^2\psi}{\partial x^2}$

$$\frac{\partial\psi}{\partial t} = 2\pi i\psi\left(-\frac{x}{\lambda^2}\frac{d\lambda}{dt} - \frac{\hbar}{m\lambda^2} + \frac{2\hbar t}{m\lambda^3}\frac{d\lambda}{dt}\right) \tag{5}$$

$$\frac{\partial^2\psi}{\partial x^2} = -4\pi^2\psi\left(\frac{1}{\lambda} - \frac{x}{\lambda^2}\frac{d\lambda}{dx} + \frac{2\hbar t}{m\lambda^3}\frac{d\lambda}{dx}\right)^2 + 2\pi i\psi\left[-\frac{2}{\lambda^2}\frac{\partial\lambda}{\partial x} + \frac{2x}{\lambda^3}\left(\frac{d\lambda}{dx}\right)^2 - \frac{6\hbar t}{m\lambda^4}\frac{d\lambda}{dx} + \frac{2\hbar t}{m\lambda^3}\frac{d^2\lambda}{dx^2}\right] \tag{6}$$

Substituting (5) and (6) into (3) and separating real and imaginary part, we will get

$$2\frac{\partial\lambda}{\partial x} - \frac{2x}{\lambda}\left(\frac{d\lambda}{dx}\right)^2 + \frac{6\hbar t}{m\lambda^2}\frac{d\lambda}{dx} = 0 \tag{7}$$



131, H.Javid ave, AZ-1143, Baku
Institute of Physics
E-mail: jophphysics@gmail.com

$$\left(\frac{x}{\lambda^2}-\frac{2\hbar t}{m\lambda^3}\right)\frac{\partial\lambda}{\partial t}=\frac{\hbar}{m\lambda^2}-\frac{2\hbar t}{m\lambda^3}\left(1-\frac{x}{\lambda}\frac{d\lambda}{dx}+\frac{2\hbar t}{m\lambda^2}\frac{d\lambda}{dx}\right)^2 \tag{8}$$

From (7) we will get

$$\frac{\partial\lambda}{\partial x}=\frac{\lambda\left(2+\frac{6\hbar t}{m\lambda^2}\right)\hbar}{x} \tag{9}$$

Substituting (9) into (8) we will get:

$$\frac{\partial\lambda}{\partial x}=-\frac{2\pi\hbar}{m\lambda A(t)}\left[1+\frac{2\lambda}{x}uA(t)+\left(\frac{\lambda}{x}\right)^2(Au)^2\right] \tag{10}$$

Here $A(t)=\frac{2\hbar t}{m\lambda^2}-\frac{x}{\lambda}$, $u=2+\frac{6\hbar t}{m\lambda^2}$

To integrate equation (10), we assume

$$\frac{2\hbar t}{m\lambda}<x,\ A=-\frac{x}{\lambda},\ u=2 \tag{11}$$

Substituting (11) into (10) we will get:

$$\frac{\partial\lambda}{\partial t}=\frac{2\pi\hbar}{mx} \tag{12}$$

From

$$\lambda=\lambda_0+\frac{2\pi\hbar t}{mx}=\lambda_0\left(1+\frac{2\pi\hbar t}{mx\lambda_0}\right) \tag{13}$$

When obtaining equation (12), we discarded the member $\frac{\partial^2\lambda}{\partial x^2}$ and this is quite justified, because, $\lambda$ depends on the coordinates like a linear way. Thus, the final energy of the wave after leaving the vacuum with size $x=L$:

$$E_{after}=\frac{2\pi^2\hbar^2}{m_0\lambda_0^2}\cdot\frac{1}{\left(1+\frac{2\pi\hbar t}{m_0\lambda_0 L}\right)^2}$$

That is why

$$\frac{E_{after}}{E_{before}}=\frac{1}{\left(1+\frac{2\pi\hbar t}{m_0\lambda_0 L}\right)^2}<<1 \tag{14}$$

Expression (14) have gotten from solving equation (10) with values for (11) $A$ and $u$. For values $A=0$ and $u=0$ $\lambda\to\infty$ and this is the classic area where the wave turns into a line. For values

$$A=\frac{2\hbar t}{m_0\lambda^2},\ u=\frac{6\hbar t}{m_0\lambda^2} \tag{15}$$

Solution of equation (10) is more complex.
Substituting (15) into (10) for wavelength we will get:

$$\lambda = \lambda_0 \left[ 1 - 2 \left( \frac{2\hbar\tau}{m_0 \lambda_0^2} \right)^2 \left( \frac{3\lambda_0}{L} \right)^2 \right]^{1/6} \tag{16}$$

And

$$\frac{E_{after}}{E_{before}} = \frac{1}{\left[ 1 - 2 \left( \frac{\hbar\tau}{m_0 \lambda_0^2} \right)^2 \left( \frac{3\lambda_0}{L} \right)^2 \right]^{1/6}} \tag{17}$$

Here, $\tau$ - the time of passing of wave through vacuum with size L.

Thus, a monochromatic wave, passing through a vacuum of length L, decreases its energy. This is the inelastic interaction of the wave with the vacuum. This means that the vacuum is not an empty means inhomogeneity. This inhomogeneity leads to losing energy of the monochromatic wave.

A wave with a longer wavelength loses more energy than a wave with a short wavelength. In addition, the wave losing energy leaves the vacuum, which means that the vacuum behaves like a massive medium in which inelastic interaction with the wave occurs. However, unfortunately, it is not known what kind of elementary particles the vacuum is filled with and they move by what law. Vacuum (emptiness) is a mysterious object in the sense of physical understanding. The properties of vacuum are not clearly defined and are closed to people

## CONCLUSION

It has been proven that a monochromatic wave, passing through a vacuum of size L, loses part of its energy. Losing energy occurs with different values of L in different ways. Vacuum is matter and has

[1] *L.D. Landau, E.M. Lifshitz.* Quantum Mechanics. Non-Relativistic Theory. Series: Theoretical physics, Moscow: Nauka, 1984, pp.13-37.

[2] *L.D. Landau, E.M. Lifshitz.* Quantum Mechanics. Non-Relativistic Theory. Series: Theoretical physics, Moscow: Nauka, 1984, pp.42-66.

[3] *L.D. Landau, E.M. Lifshitz.* Quantum Mechanics. Non-Relativistic Theory. Series: Theoretical physics, Moscow: Nauka, 1984, pp.70-100.

*Received: 08.02.2024*

# STRUCTURAL, ELECTRICAL AND OPTICAL PROPERTIES OF $Pb_{1-x}Eu_xTe$ THIN FILMS

**I.R. NURIYEV[1], A.M. NAZAROV[1], M.S. SADIGOV[1], S.S. FARZALIYEV[1], R.M. SADIGOV[1,2], V.R. ABDULSALAMOVA[1]**

*[1]Institute of Physics, Ministry of Science and Education Republic of Azerbaijan, AZ1143, H. Javid ave., 131, Baku, Azerbaijan*
*[2]Azerbaijan Technical University, Ministry of Science and Education Republic of Azerbaijan, AZ1073, H. Javid ave., 25, Baku, Azerbaijan*
*afinnazarov@yahoo.com*

Thin films of $Pb_{1-x}Eu_xTe$ solid solution was grown on freshly cleaved (111) surface of $BaF_2$ by the method of condensation of molecular beams in a vacuum of $10^{-4}$ Pa. It was shown that as grown film was (200) oriented single crystal. The type of conductivity depends on the temperature of the additional compensating source Te and at 650 K the type of conductivity changes from n to p. The smoother and uniform surface without any clusters was obtained at the deposition condition $\vartheta_c$=8÷9 Å/c, $T_{sub}$=543÷623 K. By optical measurements have been established that the produced films are direct band gap semiconductor with Eg=0.386 eV, $\alpha=10^4$ $cm^{-1}$. The energy gap of $Pb_{1-x}Eu_xTe$ (0.386 eV) is larger than that of PbTe (0.320 eV), suggesting that the energy gap can be adjusted by replacing some Te atoms with Eu.

**Keywords:** thin films, solid solutions, Semiconductor, $Pb_{1-x}Eu_xTe$, XRD, optical properties.
**PACS:** 74.25.Gz

## INTRODUCTION

In recent years, semi-magnetic semiconductor materials have been widely used and have been in the focus of researchers' attention. Semiconductor compounds of the type $A^4B^6$ (PbS, PbSe and PbTe) are characterized by a narrow band gap (Eg~0.1 eV). With the addition of rare earth elements (Eu, Mn) to these compounds, it is possible to regulate the width of the energy gap of solid solutions, which expands the scope of these materials. These solid solutions are widely used in the creation of various optoelectronic devices the properties of which can be controlled by a magnetic field.

Up to now, HgCdTe has been used as predominant material for IR detection due to its high performance [1]. But production of HgCdTe films requires an expensive technique like molecular beam epitaxy and in addition, its yield is limited by the poor mechanical stability. Because of all these, the search for the cheapest materials and technologies has yet to be carried out.

PbTe is one of the important materials with high refractive index in infrared region due to its superior chemical stability and the ease of film deposition. Band gap can be tuned by alloying it with SnTe, EuTe and i.s.

The impurity concentration dependences of the PbTe-based solid solutions parameters are well known [2-7]. By replacing part of the lead with the rare earth element Eu (creating a $Pb_{1-x}Eu_xTe$ ($0\le x\le 1$) solid solution), can be smoothly increased its band gap and reduce the refractive index.

Since the basis of the $Pb_{1-x}Eu_xTe$ ($0\le x\le 1$) solid solution is the binary compounds PbTe and EuTe, all its properties are, similar to the properties of these compounds. It is natural to assume, and this is confirmed experimentally, that solid solutions with Eu content close to zero have more similar properties to PbTe. The PbTe and EuTe compounds have the same NaCl structure type and Oh5 - Fm3m symmetry type. They have a face-centered cubic crystal lattice with very close lattice parameters $a_{PbTe}$=0.6462 nm, $a_{EuTe}$=0.6595 nm [2, 8]. Therefore, under normal conditions and at x close to zero, the $Pb_{1-x}Eu_xTe$ ($0\le x\le 1$) solid solution retains the structure of PbTe and its thin films can be produced by the method of producing PbTe thin films. For Producing PbTe films have been used a lot of technics, such as evaporation from bout, flash evaporation, hot wall-technique and so on. In this work we used the heater specially made of carbon for evaporation bulk materials with high vapor pressure.

## EXPERIMENTAL PROCEDURE

In our experiments 2-5 μm thick $Pb_{1-x}Eu_xTe$ (x=0.05) thin films were grown on freshly cleaved $BaF_2$ (111) surfaces by the condensation method of molecular beams in a vacuum of $10^{-4}$ Pa. During deposition the source and substrate temperatures were kept at $T_{sour}$=1000-1100 K and $T_{sub}$=580 K respectively. As a source materials were used synthesized at 1100 K solid solutions of $Pb_{1-x}Eu_xTe$ (x=0.05). For synthesis was used high purity (99.99%) Pb, Te and Eu. The source materials Pb and Te were etched by $CH_3COOH+H_2O_2$ (4:1) and in 20% aqueous solution of HCl respectively to remove the oxide layer. Then they were placed in quartz ampoule and evacuated to $10^{-4}$ Pa before sealing.

The ampoule was then placed in a furnace. The furnace temperature was raised to 1230 K and kept at this temperature for 30 h. For mixing of the source materials, the ampoule was slowly vibrated. Then the

131, H.Javid ave, AZ-1143, Baku
Institute of Physics
E-mail: jophphysics@gmail.com

melt was rapidly cooled down to room temperature to keep homogeneity of polycrystalline ingot.

The evaporator of the starting materials was a Knudsen cell made of especially pure graphite.

To develop the epitaxial growth technology to obtain high-quality single-crystal layers and characterize them, the following measurements were carried out: The structural property was investigated by X-Ray diffraction (XRD) analyses of the films using Bruker D2 Phaser (Germany) diffractometer in θ-2θ scan mode with Ni-filtered CuKα radiation (λ=1.54060 Å) source.

Free charge carriers concentration and mobility in the layers was determined by the Keithley Hall effect system;

Topography analysis of the films was performed in Smart SPM 1000 AIST NT (Tokyo Instruments, Japan). Elemental analyses and stoichiometry of the film were carried out using Scanning Electron Microscopy SEM S-4800 with EDX system (Hitachi Ltd., Japan). Thickness of the film was measured by ellipsometer. The optical properties of the films were studied by Fourier transform spectrometer (FTIR, Nicolet-NEXUS-870) at normal incidence.

## RESULTS AND DISCUSSION

Fig.1 shows X –ray diffraction pattern of $Pb_{1-x}Eu_xTe$ powder (a) and $Pb_{1-x}Eu_xTe$ thin film (b) on $BaF_2$. All the diffraction peaks of powdered sample correspond to $Pb_{1-x}Eu_xTe$ with lattice constant $a$=6.463 Å. We did not observe any peak corresponding to Pb, Eu or Te which conforms that the proper synthesis had been occurred. As XRD of $Pb_{1-x}Eu_xTe$ thin film contains only one (200) peak we conclude that the obtained in the given conditions films are single crystal by other word on $BaF_2$ occurred epitaxial growth of $Pb_{1-x}Eu_xTe$ thin film.

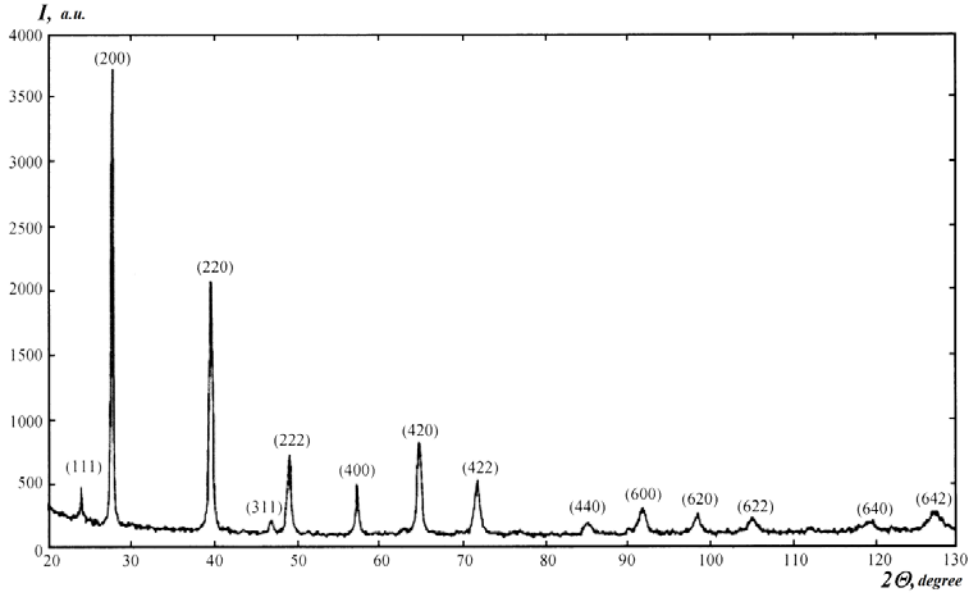


a)

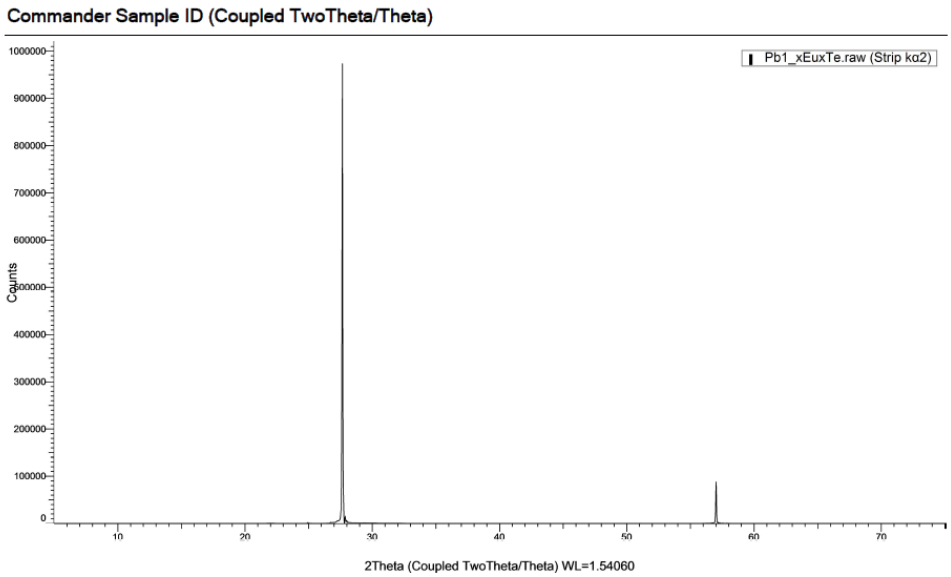


b)

*Fig.1.* XRD patterns of $Pb_{1-x}Eu_xTe$ powder (a) and thin film (b).

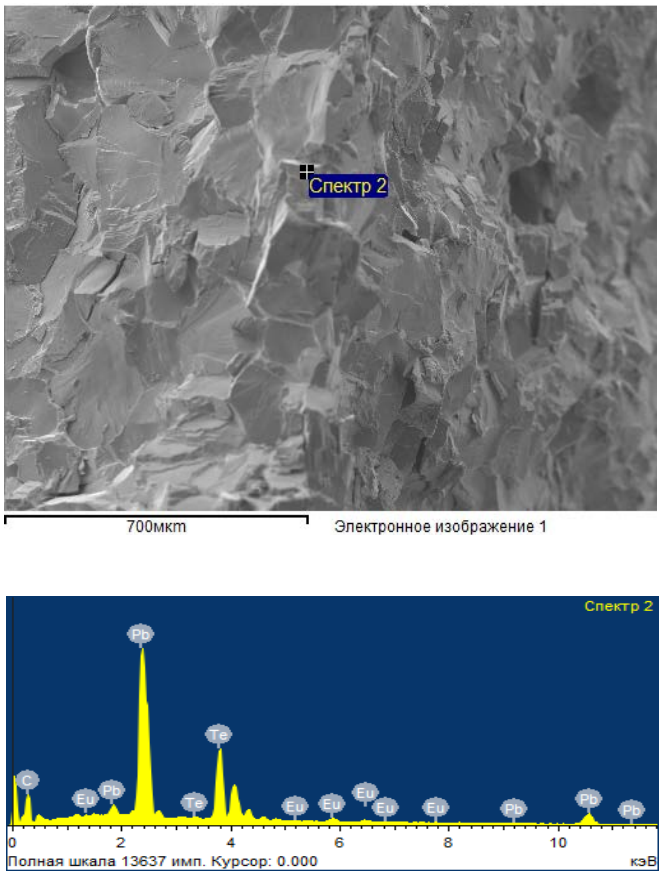


*Fig.2.* EDS measurement results of $Pb_{1-x}Eu_xTe$ thin films.

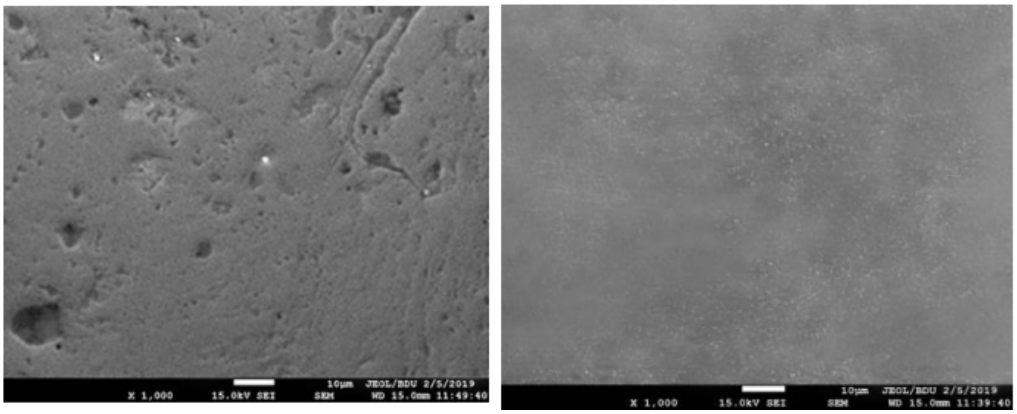

a) b)

*Fig.3.* Electron microscopic images of the surface of $Pb_{1-x}Eu_xTe$ films (x=0.05): a) without, b) with Te compensation.

The elemental composition of the film was determined by EDS spectrum. An illustration of EDS spectrum is given in Fig.2. It shows that only Pb Eu and Te are present in the film. The composition is very close to stoichiometry.

The electron microscopic images of $Pb_{1-x}Eu_xTe$ films without (a) and with Te compensation are shown in Figure 3.

On the electron microscopy images of films without Te compensation are seen black clusters characteristic for lead chalcogenides [3–5], the number of which increases with a decrease in the condensation rate and an increase in the substrate temperature (Fig.3a). According to the literature, these accumulations are oxides formed due to the capture of oxygen with excess metal atoms (Pb) during the growth process. Oxygen is captured on the surface of the films by lead atoms. Excess lead atoms are formed as a result of partial decomposition of the starting material during the deposition process. To eliminate the observed accumulations, the films were doped with an additional compensating source of Te vapor during growth. The use of such a source led, along with the disappearance of these clusters, to the production of films with a smoother surface (Fig.3b), a more perfect structure and an increased mobility of charge carriers.

It reveals that by the appearance of the surface, the smoother and uniform surface without any clusters

is obtained at the deposition condition $\vartheta_k$=8÷9 Å/c, $T_{sub}$=543÷623 K. Here $\vartheta_k$ is the rate of thin film deposition.

By adjusting the temperature of the Te compensating source, we succeeded to obtain epitaxial films of n- and p-type conductivity, with low charge carrier concentration (n, p=$2\cdot10^{18}$–$4\cdot10^{18}$ $cm^{-3}$, T=77 K) and high mobility ($\mu$=$2.5\cdot10^{3}$–$3.0\cdot10^{3}$ $cm^2/V\cdot s$, T=77 K). Conductivity inversion occurs at the temperature of the compensating source $T_{cs}$=650 K.

The optical characterization of a thin film by transmission and reflection measurements is a well-known method. Once the experimental values of R and T are known as a function of wavelength, then it is possible to calculate the absorption coefficient, the thickness and the value of the band gap width of the film.

In this work, transmission spectra measured at normal incidence were used to calculate the thickness of thin films deposited on transparent substrates. This choice of incidence direction is justified because no polarization effects appear; moreover, most commercial equipment uses this incidence direction.

The beam path in the film is shown in Fig.4. A parallel beam of light is split at both boundaries of the thin film with air and $BaF_2$ into two beams. This division occurs several times. Then the reflected or transmitted rays, overlapping, give an interference pattern. The optical path difference between the neighboring transmitted beams is 2 nd.

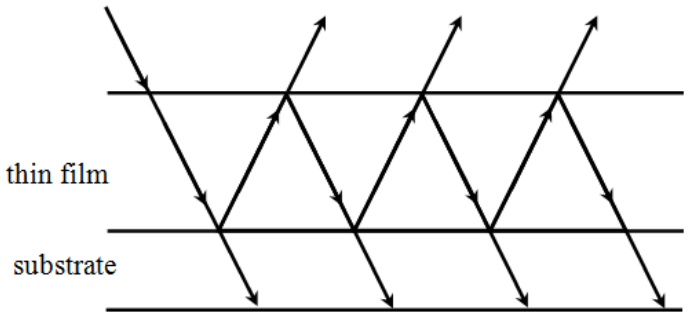


*Fig.4.* The occurrence of multiple reflections of beam in the film.

For transmitted beams the condition for constructive interference, in the case of normal incidence, is, $2nd=m\lambda_m$, where n is refractive index, m=1, 2, 3, . . . , integer numbers is interference fringes order and can be calculated by assuming that the refractive index varies slowly with the wavelength in this region. For two consecutive maximums we can write

$$2nd = m\lambda_m, \quad (1)$$

$$2nd = (m-1)\lambda_{m-1} \quad (2)$$

From these equations we fined m as

$$m= \lambda_{m-1}/ (\lambda_{m-1}- \lambda_m). \quad (3)$$

Then we calculated d by substituting m in (1) or (2).

In Fig.5 is illustrated the transmittance spectrum of $Pb_{1-x}Eu_xTe$ thin film in the range of 0-25 μm. From the interference peaks by formula (3) was calculated the thickness of film (~3 μm).

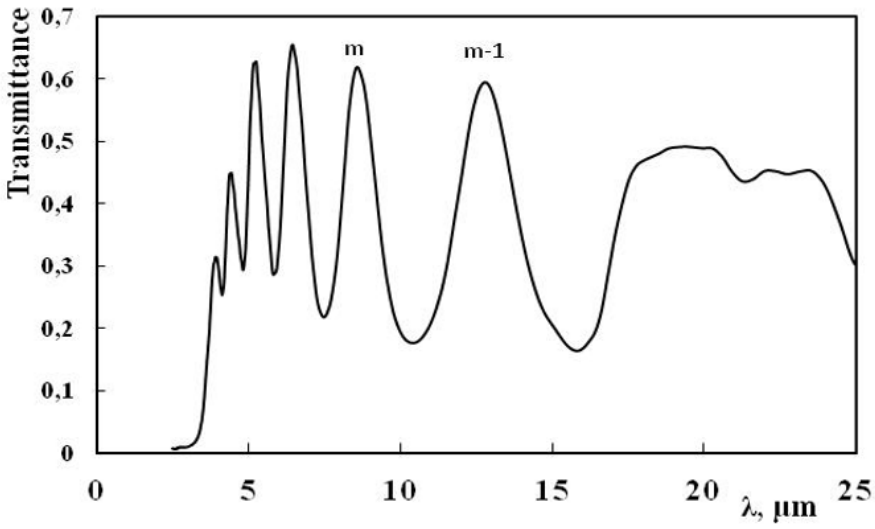


*Fig.5.* Experimental transmittance spectrum of $Pb_{1-x}Eu_xTe$ film with interference fringes.

The absorption coefficients were obtained from the transmission data using the relationship

$$T = T_0 \exp(-\alpha d), \quad (4)$$

where T and $T_0$ are the intensity of transmitted and incident beam respectively, α the absorption coefficient, and d the sample thickness. From the equation (1) α is calculated as

$$\alpha = \frac{1}{d} log \frac{T_0}{T} \quad (5)$$

It was observed that the value of absorption coefficient increases rapidly with the increase of photon energy near the fundamental absorption edge.

It is well established that the optical absorption edge in PbTe at 300 K and lower temperatures is connected with direct allowed transition between the nearest band extreme at the point L [9]. It is also known that the electronic transition between valence and conduction bands is given by Tauc's low [10]

$$\alpha h\nu = A(h\nu - E_g)^p \quad (6)$$

Where A is a constant, α the absorption coefficient, Eg the energy gap, ν the frequency of the incident beam and h the Plank's constant. The exponent p is ½ for direct allowed transitions.

We considered that the optical behavior of $Pb_{1-x}Eu_xTe$ must be very similar to that of PbTe and plotted the dependence of $(ah\nu)^2$ on $ah\nu$. This plot is shown in Fig.6.

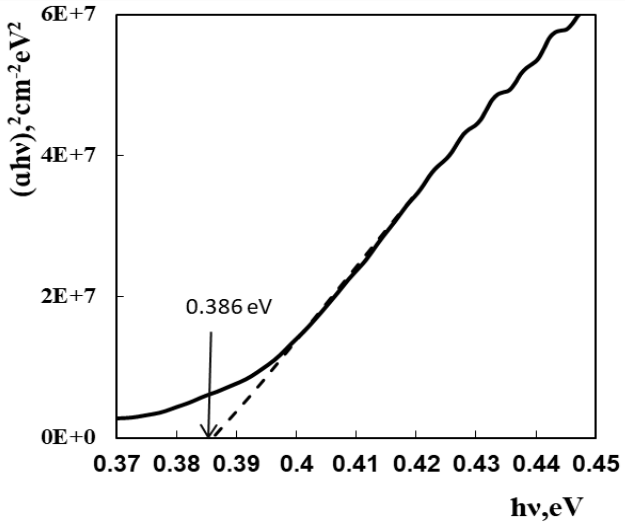


*Fig.6.* Plot of $(\alpha h\nu)^2$ versus photon energy (hν) for $Pb_{1-x}Eu_xTe$ film.

It is seen that the the plot of $(\alpha h\nu)^2$ versus photon energy (hν) is linear. By other word in equation (5) the value of p=1/2.

The single slope in the curve suggests that the prepared $Pb_{1-x}Eu_xTe$ thin film is single phase in nature and electronic transitions are direct and allowed. That is the obtained film is direct band gap semiconductor with band gap width 0.386 eV and absorption coefficient ~$10^4$ $cm^{-1}$.

The found for $Pb_{1-x}Eu_xTe$ band gap (0.386 eV) is larger than that for PbTe (0.320 eV). This result which was expected is probably associated with the presence of Eu.

## CONCLUSION

Thus, as a result of the study, the optimal conditions for obtaining $Pb_{1-x}Eu_xTe$ epitaxial films of n- and p-type conductivity with high mobilities were determined. It was fond that crustal structure of $Pb_{1-x}Eu_xTe$ is the same cubic as PbTe ($a$=6.46 Å).

It was shown that by replacing some Te atoms with Eu, the energy gap of $Pb_{1-x}Eu_xTe$ can be adjusted. The electronic transitions in $Pb_{1-x}Eu_xTe$ are direct allowed with $E_g$=0.386 eV, α=$10^4$ $cm^{-1}$. The energy gap of $Pb_{1-x}Eu_xTe$ (0.386 eV) is larger than that of PbTe (0.320 eV), suggesting that the energy gap can be adjusted by replacing some Te atoms with Eu.

[1] *Jianfei Wang, Juejun Hu, Xiaochen Sun, Anuradha M. Agarwal, Lionel C. Kimerling, Desmond R. Lim, and R. A. Synowicki.* Structural, electrical, and optical properties of thermally evaporated nanocrystalline PbTe films. Journal of Applied Physics 104, 053707, 2008.

[2] *Д.А. Пашкеев, И.И. Засавицкий.* Роль междолинного рассеяния в излучательной рекомбинации твердого раствора $Pb_{1-x}Eu_xTe$ (0<x<1). ФТП, 46 **(**2013), 745-750.

[3] *И.Р. Нуриев, С.С. Фарзалиев, Р.М. Садыгов.* Рост эпитаксиальных пленок $Pb_{1-x}Mn_xTe$ (Ga) на монокристаллах $PbTe_{1-x}Se_x$. «Поверхность». Рентгеновские,

синхротронные и нейтронные исследования. Москва, 2 (2004), 110-112.

[4] *И.Р. Нуриев, С.С. Фарзалиев, Н.В. Фараджев, Р.М. Садыгов.* Фотоэлектрические и оптические свойства эпитаксиальных пленок $Pb_{1-x}Mn_xTe$ (Ga). Прикладная физика. 4 (2006), 106-109.

[5] *Е.И. Рогачева, А.С. Сологубенко, И.М. Кривулькин.* Микротвердость полумагнитных твердых растворов $Pb_{1-x}Mn_xTe$. Неорганические материалы. 34 (1998), 669-674.

[6] *И.И. Засавицкий, Л. Ковальчик, Б.Н. Мацонашвили, А.В. Сазонов.* Фотолюминесценция полумагнитных полупроводников типа $A^{IV}B^{VI}$. ФТП, 22 (1988), 2118-2123.

[7] *И.Р. Нуриев, А.М. Назаров, Р.М. Садыгов, С.С. Фарзалиев, М.С. Садыгов.* Рост и структура эпитаксиальных пленок $Pb_{1-x}Eu_xTe$. AMEA Xəbərlər, 2022, №2, 121-124.

[8] *А.В. Голубков, Е.В. Гончарова, В.И. Жузе, Г.М. Логинов, В.М. Сергеева, И.А. Смирнов.* Физические свойства халькогенидов редкоземельных элементов. Ленинград: Наука, 1973, 238-290.

[9] *Paul Biplab, P. Banrji.* Optical and electrical properties of as-grown single crustalline PbTe. Journal of Crystal Growth. 311(2009) 1260-1263.

[10] *Lakshmanan Kungumadevi and Ramakrishnan Sathyamoorthy.* Structural, Electrical, and Optical Properties of PbTe Thin Films Prepared by Simple Flash Evaporation Method. Advances in Condensed Matter Physics, 2012 (2012), 1-5.

*Received: 29.02.2024*

# ON THE PHYSICAL MECHANISM OF QUANTUM JUMPS IN ATOMS

**AZAD Ch. IZMAILOV**
*Institute of Physics, Azerbaijan Republic Ministry of Sciences and Education,*
*Baku, AZ-1143, Azerbaijan*
*e-mail: azizm57@rambler.ru*

The possible mechanism of quantum jumps in hydrogen-like atoms as a consequence of the processes of inelastic scattering of an atomic electron on a nucleus inside an atom is discussed. Such processes can occur due to the specific internal structure of the proton. The direct connection has been established between spontaneous transitions in atoms and the quantum jumps under consideration.

**Keywords:** quantum jumps, inelastic scattering, proton, atomic spontaneous transitions.
**PACS:** 32.30.-r, 42.50.Lc

## 1. INTRODUCTION

Quantum jumps in various atomic systems have been the objects of active fundamental research since the beginning of quantum mechanics [1, 2]. Recently, in connection with the development of attosecond technology and spectroscopy [3], significant progress has been made in studying the dynamics of such short-time processes [4, 5]. However, the physical mechanism of these quantum jumps in atoms is not yet clear. This work discusses such a possible mechanism, which is associated with the processes of inelastic scattering of atomic electrons by the nucleus inside the atom. The consideration was carried out for hydrogen-like atoms, which consist of a single electron and a positively charged nucleus. These, in addition to the hydrogen atom, also include ions of elements such as $He^{+}$, $Li^{2+}$, $Be^{3+}$, etc.

The next section presents the qualitative rationale for this mechanism based on the brief historical overview of development of atomic models. Next (in Section 3) a number of simple relationships are obtained for the spontaneous decay of excited atomic states by means of the quantum jumps under consideration. The final Section 4 presents the main conclusions of this work.

## 2. QUALITATIVE RATIONALE

It is well known that the classical Rutherford model of the atom turned out to be untenable due to the inevitable and very rapid (within nanoseconds) fall of an atomic electron onto the nucleus due to the radiation of this electron during its accelerated motion. In subsequent Bohr's model of the atom, it was assumed that atomic electrons could move only in certain orbits spatially distant from the atomic nucleus [1,2,6]. Thus, the possibility of atomic electrons falling onto the nucleus was denied, because then the “collapse” of the atomic system was assumed. Indeed, such a “collapse” occurs, for example, in the case of such a hydrogen-like system as positronium, which consists of two structureless antiparticles (electron and positron). Due to the approach of these oppositely charged antiparticles, their annihilation occurs within nanoseconds [7].

According to the modern quantum model of the atom, based on the Schrödinger equation, quantum states of the atomic electrons are described by wave functions that can have non-zero values throughout the entire volume of the atom, including its nucleus [6]. However, during the development of this quantum model, in particular for the simplest hydrogen atom, it was assumed that the electron, during its movement inside the atom, does not directly collide with the nucleus (proton). This assumption was associated primarily with the negligibly small region of the atomic nucleus compared to the characteristic dimensions of the atom. In addition, for example, in the case of the hydrogen atom, it was assumed that its nucleus (proton) is a structureless particle. Therefore, the corresponding Schrödinger equation for the hydrogen atom was solved with respect to the wave function of the electron moving in the Coulomb field of the point nucleus [6]. Thus, stationary quantum states of an atomic electron with certain values of the total energy and angular momentum of this electron were determined [6]. Formally, such excited states of an atomic electron can exist unlimited time, although in reality they spontaneously decay to lower quantum levels down to the ground atomic term. Subsequently, this spontaneous decay of excited states of the atom was described within the framework of quantum electrodynamics based on possible fluctuations of the electromagnetic vacuum [8].

Meanwhile, by the mid-seventies of the last century, fundamental experiments were carried out on the bombardment of protons with fast electrons [9]. Based on the analysis of the observed processes of elastic and inelastic electron scattering in these experiments, a rather complex internal structure of the proton, consisting of quarks and gluons, was established [9, 10]. State of such a proton structure can change significantly under the influence of various elementary particles, including electrons. It is obvious that in the hydrogen atom, due to the Coulomb attraction, the electron will inevitably approach the nucleus until it reaches nuclear gluon-quark structure, where, in addition to the electromagnetic interaction, the strong interaction between elementary particles also becomes significant. However, in contrast to the mentioned case of positronium [7], instead of



131, H.Javid ave, AZ-1143, Baku
Institute of Physics
E-mail: jophphysics@gmail.com

annihilation, processes of elastic and inelastic scattering of the electron on the proton inside the atom will occur. Such a scattering should lead to a redistribution of energy and angular momentum between the atomic electron and the nucleus. These processes were not taken into account in the corresponding Schrödinger equations, compiled only for the electron wave functions, without a possible associated change in the internal state of the atomic nucleus [6]. It is obvious that the considered processes of electron scattering on a nucleus will be very short-time compared to a duration of the atomic electron's stay in an excited state, since the characteristic dimensions of an atom are many times greater than the effective dimensions of its nucleus. However, it is precisely such abrupt processes of inelastic scattering of an atomic electron on a nucleus that can lead to observed spontaneous transitions in the atom between electronic quantum states with different energies, accompanied by the emission of photons of corresponding frequencies.

Of course, correct consideration of such inelastic scattering of the atomic electron on the nucleus will greatly complicate the solution of the corresponding problem even for the hydrogen atom. Then it will be necessary to solve interrelated equations for the quantum states of the electron and nucleus, taking into account possible changes in the internal structure of the nucleus, which are not yet fully known. Apparently, this will require additional experimental and theoretical studies.

At the same time, in the next section some simple relations will be obtained for the process of spontaneous decay of excited states of an atomic electron as a result of the quantum jumps under consideration.

## 3. SPONTANEOUS DECAY OF EXCITED ELECTRONIC STATES

Let us consider the excited electronic state $|e\rangle$ of an individual hydrogen-like atom, created at time $t = 0$. It is believed that after some time $\tau \geq 0$, an abrupt decay of this state into lower energy levels of the electron occurs. Assuming such a quantum jump to be instantaneous, we can write the following expression for the population $p$ of the state $|e\rangle$:

$$p(t) = \eta(\tau - t), \tag{1}$$

where $\eta(\tau - t)$ is the step function (see figure).

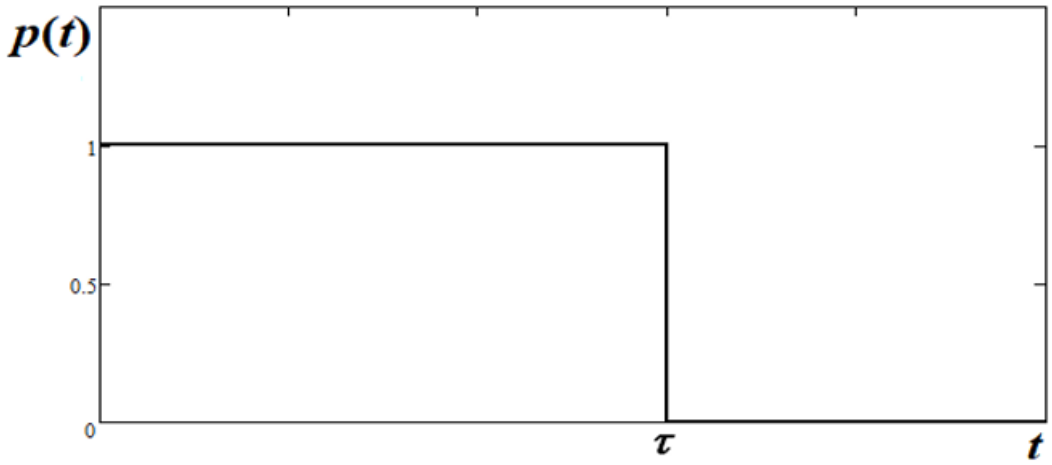


*Fig.* Time dependence of the population $p(t)$ of the excited state $|e\rangle$ of the atomic electron, starting from its appearance at the moment $t = 0$ until its spontaneous decay as a result of a quantum jump at the moment t=τ

An ensemble of a sufficiently large number of atoms $N$ excited to the state $|e\rangle$ at the moment $t = 0$ decays spontaneously according to the well-known law [6]:

$$N(t) = N_0 exp(-\gamma t), \tag{2}$$

where $N_0$ is the number of such atoms at the initial moment $t = 0$, and $\gamma$ is the radiative damping constant.

At the same time, the dynamics of changes in the population of such an ensemble of excited atoms as a result of the quantum jumps under consideration (1) is also described by the following relation:

$$N(t) = N_0 \int_0^\infty \eta(\tau - t) f(\tau)\, d\tau = N_0 \int_t^\infty f(\tau)\, d\tau. \tag{3}$$

Here $f(\tau)$ is the distribution function over time moments $\tau$ of quantum jumps in individual atoms, which is easily determined from the equality of expressions (2) and (3):

$$f(\tau) = \gamma exp(-\gamma\tau), \quad (\tau \geq 0\ ). \tag{4}$$

According to the distribution (4), the characteristic lifetime $\gamma^{-1}$ of the excited state $|e\rangle$ can also be interpreted as the interval of time during which the spontaneous decay of this state $|e\rangle$, by means of considered quantum jumps, is most probable. It is obvious that this time $\gamma^{-1}$, associated with the dynamics of the motion of the electron in the state $|e\rangle$ throughout atomic volume, is many times greater than the duration of the quantum jump under consideration,

due to the very short-time process of inelastic scattering of this electron directly in the region of the atomic nucleus. This circumstance, in particular, can qualitatively explain the increase in the lifetime of excited Rydberg atoms with increasing their sizes [11]. Indeed, then a relative volume of the nucleus in the atom, where the quantum jumps in question can occur, decreases.

Note that after the aforementioned radiative decay of the excited electronic state $|e\rangle$ into some lower energy quantum levels, these levels will further decay in a similar way by means of considered quantum jumps until the atom reaches the ground stable quantum state.

It was noted above that the radiative decay constant $\gamma$ (4) of the excited electronic state of an individual atom was previously calculated by methods of quantum electrodynamics within the framework of the concept of the electromagnetic vacuum [8]. At the same time, according to my analysis, this constant $\gamma$ may be determined directly by probabilities of inelastic scattering of an excited atomic electron on the nucleus inside the atom.

## 4. CONCLUSION

According to the above arguments, very short-time quantum jumps, that occur during the spontaneous decay of an atom, can be caused by inelastic collisions of an excited electron of this atom with its nucleus. As a result, spontaneous transitions take place in the atom between electronic quantum states of different energies with the emission of recorded photons of the corresponding frequencies.

It is important to note that during such jumps not only sharp changes in the energy of an atomic electron can occur, but also an exchange of its angular momentum with the atomic nucleus. This phenomenon, in particular, can change the established concept of the total angular momentum of an atomic electron as the sum of its orbital momentum and its spin.

In my opinion, further more detailed study of the considered jump-like processes of scattering of bound electrons in an atom on its nucleus will make it possible to present a more correct physical interpretation of observed phenomena in atomic spectroscopy.


[1] *J.E. Baggott.* The Quantum Story: A History in 40 Moments. Oxford University Press (2011).

[2] *Carl S. Helrich.* The Quantum Theory—Origins and Ideas: A Historical Primer for Physics Students. Springer (2021).

[3] *Thomas Schultz, Marc Vrakking.* Attosecond and XUV Physics: Ultrafast Dynamics and Spectroscopy. John Wiley & Sons (2013).

[4] *W.M. Itano, J.C. Bergquist, D.J. Wineland.* Early observations of macroscopic quantum jumps in single atoms. International Journal of Mass Spectrometry, Volume 377, pp. 403-409 (2015).

[5] *Z.K. Minev, et al.* To catch and reverse a quantum jump mid-flight. Nature 570, pp. 200–204 (2019).

[6] C.J. Foot. Atomic Physics. Oxford University Press (2005).

[7] *O.E. Mogensen*. Positron Annihilation in Chemistry. Springer Berlin Heidelberg (2012).

[8] *Ulrich D Jentschura, Gregory S Adkins.* Quantum Electrodynamics: Atoms, Lasers and Gravity. World Scientific Publishing (2022).

[9] *R.J. Roberts.* The structure of the proton: Deep Inelastic Scattering. Cambridge University Press (1990).

[10] *M. Y. Han.* Quarks and Gluons: A Century of Particle Charges. World Scientific Publishing (1999).

[11] *Thomas F. Gallagher. Rydberg Atoms.* Cambridge University Press (2005).


*Received: 05.03.2024*

# ELECTRET PROPERTIES OF $ZrO_2$ NANOPARTICLES – POLYPROPYLENE COMPOSITES

**T.D. IBRAHIMOV, H.S. IBRAHIMOVA**
*Institute of Physics, Ministry of Science and Education of Azerbaijan, Baku, Azerbaijan, G.Javid ave. 131, AZ1143*
*Hicran90@rambler.ru*

Polypropylene samples with the additive of $ZrO_2$ nanoparticles at concentration of 3 vol.%, at which the highest electret properties are observed, have been studied by the thermally stimulated depolarization (TSD) current method at different intensities ($5\cdot10^6$ V/m, $10^7$ V/m and $1.5\cdot10^7$ V/m) of pre-applied electrostatic field. The measurement of TSD currents revealed the presence of two main peaks in the spectra of the nanocomposite at 25-35°C and 120 -140°C. They appear as a result of destruction of one or another category of traps of injected charges. Calculations have shown that there is a monomolecular mechanism of charge recombination in these nanocomposites. It is shown that increasing the applied electric field leads to an increase in the intensity of the termograms, reaching a maximum at $10^7$ V/m and then decreasing at 1.5-$10^7$ V/m. The activation energy, the total accumulated charge and the relaxation time behave similarly.

**Keywords:** polypropylene; zirconium dioxide; nanocomposite; charge recombination; thermally stimulated depolarization curren; monomolecular and bimolecular mechanism
**PACS:** 61.46.w,82.35:Np.71.38.k

## INTRODUCTION

In recent years, there has been an increased interest in obtaining polymer electrets with the highest charge storage capability and stability. The range of use of electrets extends from household appliances to special-purpose equipment. The possibility of regulating the electret properties of polymers by adding fillers to the initial polymer matrix is of sufficient interest [1, 2, 3]. The use of metaloxide nanoparticles for modification of polymers makes it possible to significantly improve a number of properties of polymer compositions, in particular, deformation and strength, fire resistance, electrical conductivity and thermal conductivity [4, 5]. During operation, devices with elements made of polymer nanocomposites are subjected to prolonged exposure to electric fields [6,7]. The use of external fields and radiation (electric field exposure, corona discharge, electron or ion bombardment, laser and X-ray radiation) contributes to an increase in the electret effect of polymer composites due to the formation of active functional groups in the structure [8, 9]. Earlier we have shown that at a concentration of 3 vol.% $ZrO_2$ in polypropylene an increase in electret properties is observed [10].

The aim of this work is to establish the mechanism of electric field effect on the electret properties of polypropylene with a concentration of 3 vol.% $ZrO_2$ nanoparticles.

## EXPERIMENTAL

The isotactic polypropylene (PP) granules with dimensions of 5 mm (Dema Import and Export Co. Ltd., China) were used to make the matrix.

Granules were dissolved in toluene at 120°C. The zirconium dioxide particles with sizes of 20-25 nm of the monoclinic phase (Sigma-Aldrich, USA) stabilized by yttrium oxide were added into the mixture and shaken for 1 h using a magnetic mixer. The solution is subjected to thermal treatment for 3-6 hours. To remove free solvents from the solution obtained, it is treated under vacuum conditions. After drying of toluene in fume hood, the composites with zirconium dioxide of 3 vol.% were obtained.

Disc-shaped samples of composites were obtained by hot pressing at temperature of 175°C and pressure of 15 MPa. Pressing time after reaching the selected temperature was 3 min. The diameter and thickness of the obtained films were 4 cm and 80-90 μm, respectively.

The samples were subjected to the electrostatic field with different intensity ($5\cdot10^6$ V/m, $10^7$ V/m and $1.5\cdot10^7$ V/m) at room temperature for 1 h. A high-voltage rectifier (VSM-989, Russia) was used as a voltage source.

The charge states were studied by the method of thermally stimulated depolarization (TSD). In order to measure currents, the samples were placed in the grounded heated cell of the sandwich type with clamping stainless steel electrodes. The electrodes were connected to the electrometric amplifier U5-11 (firm MNIPI, Russia) the output of which was attached to the two-coordinate recorder (Endim 620.02, firm RFT, Germany). The measurements of TSD currents depending on temperature were carried out in the temperature range of 0-230°C with a linear increase in temperature at the rate of 4 degrees/min.

The activation energy was calculated by using initial rise method [11]. The total charge $Q$ is defined as:

$$Q = \frac{1}{\beta}\int_{T_1}^{T_2} I(T)dT, \qquad (1)$$

where $T_1$ and $T_2$ are the lower and upper temperature limits for the existence of this charge, $\beta$ is the rate of linear heating process.

## RESULTS AND DISCUSSIONS

Fig. 1 shows the thermograms of depolarisation currents in the temperature range 0°C-200°C of PP+3%$ZrO_2$ nanocomposites, which were subjected to

131, H.Javid ave, AZ-1143, Baku
Institute of Physics
E-mail: jophphysics@gmail.com

the preliminary action of electrostatic field of different intensity at room temperature.

As shown in the figure, the measurement of thermally stimulated depolarization currents revealed the presence of two main peaks in the spectra of the nanocomposite at 25-35°C and at 120 -140°C. It indicates the existence of a complex mechanism of charge transfer and relaxation processes in the considered system. The formation of dominant maxima in the spectra of thermally stimulated currents is caused by the formation and disappearance of structural charged defects that were in potential traps before the thermal activation process. They appear as a result of destruction of one or another category of traps of injected charges. In our nonpolar matrix, the stability of the electret state is determined by localized states (traps) on the surface. Surface traps are often energetically deeper than bulk traps. As a result, homocharge accumulates on surface traps and is efficiently retained by them. The maximum in the low-temperature region is due to the emptying of traps at the interface between the amorphous and crystalline phases of the matrix. [12]. The release of charge carriers from the traps located at the interface between the matrix and the filler, accompanied by an intense movement of the end groups, double bonds and oxidised fragments of the macromolecules, is registered in the TST spectrum in the form of a high temperature peak. [13]

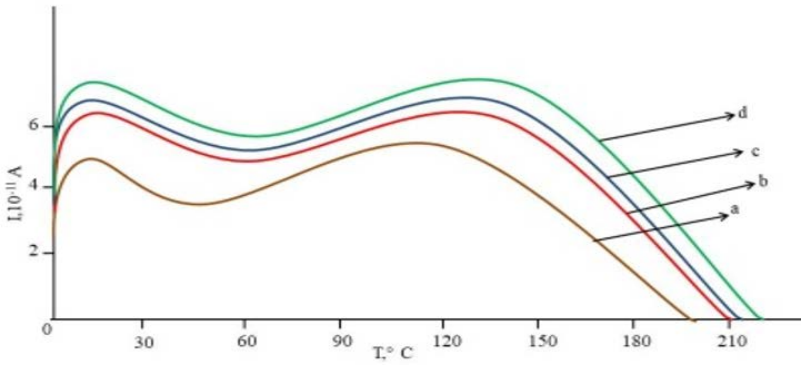


*Fig. 1.* TSD thermograms for PP+3%$ZrO_2$ nanocomposites subjected to the preliminary action of electrostatic field of different intensity at room temperature: (a) 0; (b) $5 \cdot 10^6$ V/m; (c)$10^7$ V/m; (d) $1.5 \cdot 10^7$ V/m.

The mechanism influencing the charge capture and release processes in nanocomposites is defined as follows. The criterion for determining the mechanism of charge recombination is the relation [14]:

$$\delta = \frac{T_2 - T_m}{T_2 - T_1} \qquad (2)$$

where $T_m$ is the temperature corresponding to the maximum of the depolarization current, $T_1$ and $T_2$ are absolute temperatures at which the TSD peak has half the magnitude of the peak maximum on the low and high temperature sides, respectively.

To satisfy the monomolecular recombination mechanism, the following relationship must be fulfilled:

$$\delta \leq \frac{1}{e}\left[1 + \frac{2KT}{E}\right] \qquad (3)$$

While the opposite applies to the bimolecular mechanism, namely:

$$\delta \geq \frac{1}{e}\left[1 + \frac{2kT}{E}\right] \qquad (4)$$

where $e$ is base of natural logarithm, $k$ is Boltzmann constant; $E$ is activation Calculations have shown that there is a monomolecular mechanism of charge recombination in these nanocomposites.

Electrical treatment has a noticeable effect on the thermograms. Increasing the applied electric field leads to an increase in the intensity of the low and high temperature peaks. In addition, the high temperature peak shifts towards high temperatures while the low temperature peak shifts towards low temperatures. It is attributed to the change in crystallinity, Electrical treatment not only increases the number of charge traps, but also favours a greater depth of their occurrence, which in turn provides greater stability of the charges. Charges are injected into the composite during the polarization process from the inter-electrode spaces and from the electrodes [15]. As the polarisation voltage increases, the values of electret properties increase due to the increase in the number of injected carriers trapped inside the material. In addition, the mobility of macromolecules adsorbed on the filler is limited, which allows the charge to be more stable. At low field intensity applied to the sample, the charges coming out of the traps accumulate. It, in turn, creates a local internal field. When the field intensity $15 \cdot 10^6$ V/m is applied, a local field of maximum intensity is formed, which prevents the charges from leaving the traps. As a result, the intensity of the thermogram decreases. This agrees with the results of calculation of the accumulated volume charge depending on the applied voltage (Fig. 3).

Fig. 3 shows the dependence of the activation energy W of the release of charges from the traps, as well as the temperature of the maxima of the TSD peaks, as a function of the intensity of the electrical treatment. The activation energy represents the depth of the traps, i.e. the potential barrier that the charges have

to overcome when leaving the traps. As can be seen, the activation energy increases with increasing applied electric field, reaching a maximum value at $10^7$ V/m and then decreasing at field intensity $1{,}5 \cdot 10^7$ V/m. Such a dependence of the activation energy is in agreement with the results of calculations of the dependence of the accumulated volume charge on the applied field. As can be seen from the same figure, the temperature of the thermogram maxima is synchronized with the course of the activation energy curves. In fact, according to [16], the dependence between the activation energy and the temperature of the thermogram peak has the following form

$$E_t = 25kT_m \quad (5)$$

That is, the change in activation energy is directly proportional to the peak temperature of the thermogram.

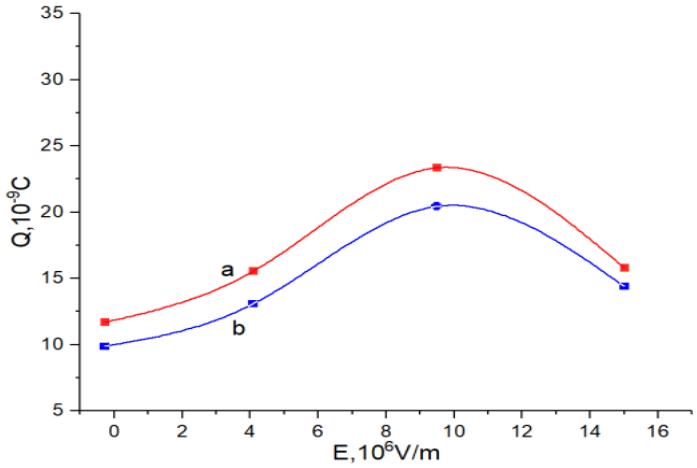


*Fig. 2.* Dependence of the magnitude of volume charges accumulated in the traps of the composite with the concentration of 3 vol.% $ZrO_2$ on the external electric field intensity: (a) charges accumulated by the traps corresponding to the high-temperature peak; (b) charges accumulated by the traps corresponding to the low-temperature peak. As can be seen from this figure, the magnitude of the accumulated charges increases with increasing field, reaching its maximum value at field intensity $10^7$ V/m. Further increase of the external field strength leads to decrease of the accumulated charge.

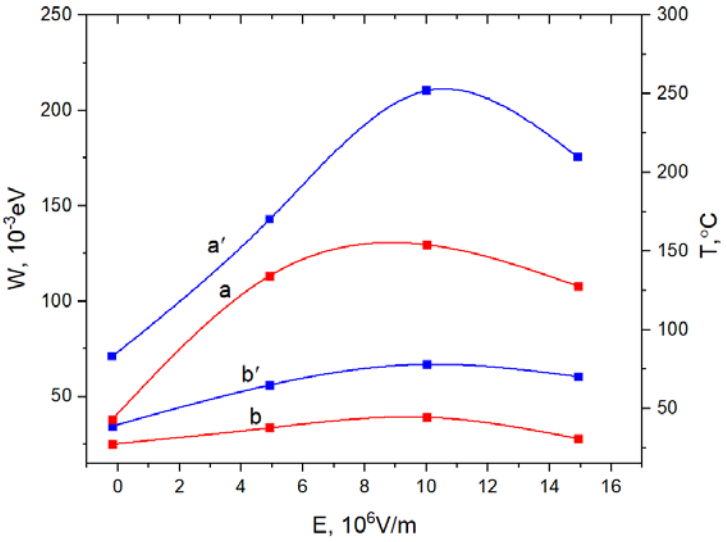


*Fig. 3.* Temperature of the maxima of the TSD peaks and activation energy W of charge release from traps as a function of the applied electric field intensity:

The magnitude of the charge is due to the amount of injected charge carriers trapped in deep bulk traps. The magnitude of the electret characteristics of polymers depends on the amount of injected charge carriers penetrating into the material during polarization fixed on energy traps of different nature.

The surface potential V as a function of time is well described by an exponential function of the form:

$$V_c = V_0 \exp(-t/\tau), \quad (6)$$

where $V_0$ is initial value of the surface potential; $\tau$ is the relaxation time; t is time.

Relaxation time characterises the ability of an electret sample to retain charge over time. It depends on various factors. In particular, on the diffusion of charges inside the sample. In this case, the surface potential decreases.

Another reason for the decrease of the surface potential is the recombination of charges. In addition, the relaxation time is also influenced by the environment, temperature, and electron-ion processes. Calculations of the relaxation time according to the relation (6) are given in the form of points in Fig. 4.

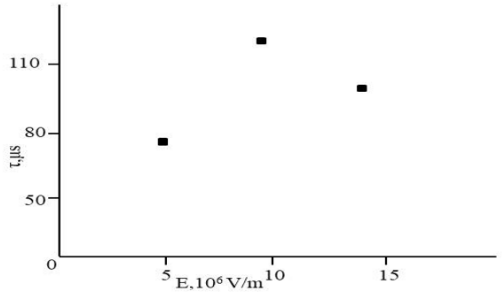


*Fig.4.* Relaxation time dependence on the intensity of the pre-applied field.

As can be seen, the maximum value of relaxation time is observed at the pre-exposure of an electric field with an intensity of $10^7$ V/m. It is at this intensity of the field applied to the sample that greater electret durability of the nanocomposite sample is observed.

## CONCLUSION

It is shown that increasing the applied electric field leads to an increase in the intensity of the termograms, reaching a maximum at $10^7$ V/m and then decreasing at $1.5 \cdot 10^7$ V/m. The activation energy, the total accumulated charge and the relaxation time behave similarly. This is due to the increase in injected charges, but at higher field intensity of an internal field is formed which prevents this process.

In other words, the highest and most stable electret properties in the investigated nanocomposites are formed under the pre-exposure to an electric field with an intensity of $10^7$ V/m


[1] *Xiang Xi, D.D.L. Chung.* Electret behavior of carbon fiber structural composites with carbon and polymer matrices, and its application in self-sensing and self-powering Carbon 160, 2020, 361e389. https://doi.org/10.1016/j.carbon.2020.01.035

[2] *D.D.L. Chung*. A review of multifunctional polymer-matrix structural composites Composites Part B 160, 2019, 644–660. https://doi.org/10.1016/j.compositesb.2018.12.117

[3] *G. A. Kontos1, A. L. Soulintzis1, P. K. Karahaliou1, G. C. Psarras, S. N. Georga1, C. A. Krontiras, M. N. Pisanias*. Electrical relaxation dynamics in $TiO_2$ – polymer matrix composites EXPRESS Polymer Letters Vol.1, № 12, 2007, 781–789. DOI: 10.3144/expresspolymlett.2007.108

[4] *N. Vidakis, M. Petousis, E. Velidakis, L.Tzounis, N Mountakis, AKorlos, P.E.Fischer-Griffiths and S. Grammatikos.* On the Mechanical Response of Silicon Dioxide Nanofiller Concentration on Fused Filament Fabrication 3D Printed Isotactic Polypropylene Nanocomposites) Polymers 2021, 13, 2029. https:// doi.org/10.3390/polym13122029

[5] *M.M. El-Desoky, I. Morad, M.H, Wasfy & A.F. Mansour*. Synthesis, structural and electrical properties of PVA/$TiO_2$ nanocomposite films with different $TiO_2$ phases prepared by sol–gel technique. Journal of Materials Science: Materials in lectronics2020. doi:10.1007/s10854-020-04313-7

[6] *A.T.Ponomarenko, A.R.Tameev, V.G. Shevchenko.* Synthesis of polymers and modification of polymeric materials in electromagnetic fields Russian Chemical Reviews, 2018, 87 (10), 923–949 DOI: https://doi.org/10.1070/RCR4790

[7] *D.N. Sadovnichii, A.P. Tyutnev, Yu.M. Milekhin.* Electrical effects in polymers and composite materials under electron beam irradiation, Russ Chem Bull, 2020, Vol. 69, Iss. 9, P. 1607, DOI: 10.1007/s11172-020-2944-y.

[8] *U. Mescheder, B. Muller, S. Baborie and P. Urbanovic.* Properties of $SiO_2$ electret films charged by ion implantation for MEMS-based energy harvesting systems JOURNAL OF MICROMECHANICS AND MICROENGINEERING 19, 2009. 094003DOI:10.1088/0960-1317/19/9/094003

[9] *O. Gradov, M. Gradova, S.N. Kholuiskaya, A.A. Olkhov*. Electron Plasma Charging Effects on the Biocompatible Electrospun Dielectric Fibers 2022, IEEE Transactions on Plasma Science 50(1):176-186 DOI:10.1109/TPS.2021.3130854

[10] *M.A. Ramazanov, H.S. Ibrahimova, H.A. Shirinova.* Influence of temperature-time crystallization conditions on PP + $ZrO_2$ charge state and electret properties Ferroelectrics 577 (1), 153-160/ https://doi.org/10.1080/00150193.2021.1916358

[11] *M.Karmakar*. On the Initial Rise Method for Kinetic Analysis in Thermally Stimulated Luminescence. Indian Journal of Science and Technology, 5(11), 2012, 3674-3677.

[12] *Bin Dang, Jinliang He, Jun Hu and Yao Zhou.* Large improvement in trap level and space charge distribution of polypropylene by enhancing the crystalline − amorphous interface effect in blends Polym Int 2016; 65: 371–379 DOI 10.1002/pi.5063

[13] *M. Szuwarzyński, K. Wolski, T. Kruk, S. Zapotocznyb.* Macromolecular strategies for transporting electrons and excitation energy in ordered polymer layers Progress in Polymer Science 121:101433 DOI:10.1016/j.progpolymsci.2021.101433

[14] *E.G. Asadov, F.A. Kazimova, T.Sh. Ibragimova , K.O. Tagiev.* Thermostimulated luminescenceof $Ca(A_{1x}Ga_{1-})_2S_4Eu_2$+crystals

Technical Physics Letters Volume 43, pages 201–204, 2017.
https://doi.org/10.1134/S1063785017020158

[15] *V.A. Goldade, S.V. Zotov, V.M. Shapovalov, V.E. Yudin*. 2019 Electret effect in polymer nanocomposites (review). Polymer Materials and Technologies, 5, 6-18. DOI: 10.32864/polymmattech-2019-5-2-6-18

[16] *Z. Jelcic.* Thermally Stimulated Depolarization of Polymers.Polimeri, , 8, 1987, 265-268.

*Received: 15.03.2024*

# PHOTOLUMINESCENCE OF NANOCRYSTALS OF $LaPO_4:Eu^{3+}$

**O.B. TAGIEV[1,2], E.G. ASADOV[1,3], F.A. KAZIMOVA[1]**
*[1]Institute of Physics of ARETN, Baku, Azerbaijan*
*[2]Moscow State University, Baku Branch, Baku, Azerbaijan*
*[3]National Aviation Academy, Baku, Azerbaijan*
*e-mail: elsenesedov@gmail.com*

The results of studying the luminescence spectra and its excitation, as well as the luminescence kinetics of the $LaPO_4:Eu^{3+}$ crystal are presented in this paper. Excitation spectra was measured under 337 nm nitrogen laser source and all observed peaks in the range of 230–460 nm were explained by electronic transition of $Eu^{3+}$ ions as well as $LaPO_4$ matrix. Photoluminescence measurements were performed at 337 nm and 393 nm wavelengths for different $Eu^{3+}$ concentrations. Obtained results are comparatively presented. All PL peaks observed in the visible range of the light are explained by electronic transition of $Eu^{3+}$ ions and $LaPO_4$ matrix. Moreover, The emission decay kinetics for the maximum at 590 nm ($^5D_0 \rightarrow {}^7F_1$) were performed under 393 nm pulsed laser and the lifetime of electrons in the traps have been determined.

**Keywords**: Luminescence, nanocrystals, spectra, excitations, lifetime.
**PACS:** 76.30.,78.55.,78.60.

## INTRODUCTION

Rare-earth doped materials are widely investigated by world scientist due to very interesting physical properties, in particular optical properties. These ions create a local emission centers when introduced in host matrix and make a significant changes in physical properties. In particular, rare-earth doped sulfides and oxide[1-4] exhibit high PL emission in the visible region of light which promises great application prospects. Therefore, rare-earth doped materials are traditionally used as phosphors for white LEDs, lasers, displays etc. Depending on the application area, different materials can be a good candidate which used as active media for mentioned areas. Among them, rare-earth doped alkaline earth thiogallates should be especially noted due to very interesting optical properties. Wide bandgap, high emission intensity, high efficiency, extreme stability of photoluminescence spectra in wide range of excitation power density and high stability are characteristic properties these types of materials [5-7]. Although these materials are investigated since the 1970s, new combinations and new characteristics increase interest in these materials day by day. Until recent years, binary and ternary compounds of these types of materials were intensively investigated by world scientists [6-13]. However, it has become known in recent years that more interesting optical properties are observed when alkaline earth ions (or cations) are partially substituted with others. By this way, emission properties can be controlled in the certain wavelength interval.

## EXPERIMENTAL

Nanocrystalline orthophosphates were obtained by precipitation with disubstituted ammonium orthophosphate at room temperature from aqueous solutions of nitrate salts of the corresponding metals at pH about 7 [14]. The precipitates were kept in the matrix solution for a day, after which they were washed by decantation, filtered, and dried in air at 110°C.

X-ray phase analysis was carried out using powder diffraction patterns obtained on a DRON-3 X-ray diffractometer (CuKα radiation). These compounds crystallize in the hexagonal crystal system and contain from 0.5 to 3 mol $H_2O$ per formal unit. When heated, they lose water and transform into a monoclinic form of a monazite-type mineral [15].

The size of the nanoparticles was determined by the broadening of the diffraction peaks according to the Scherrer formula and by the method of an EM-125 transmission electron microscope (Usc=75kV).

Photon excitation λ=393 nm was obtained from two types of laser systems: with a pulsed nitrogen laser (Lazer Photonics LN1000, pulse energy - 0.14mJ, pulse frequency 0.6ns) and a dye laser (Lazer Photonics LN 102, RVVO). The reflected beam from the sample was collected using an optical fiber receiver located at a distance of 10 mm perpendicular to the sample surface and analyzed using a spectrometer (Jobin-Ivon Spektrometer HR 460) and a multichannel SDS charge detector for the visible and near-infrared regions of the spectrum. The attenuation spectra were analyzed using a PM Hamamatsu R928 spectrometer for the visible region. Photoluminescence curves were recorded using a PM Hamamatsu R5600 U and Tektronix TDC 784A with a time constant of about 1 ns.

## RESULTS AND DISCUSSION

The excitation spectrum of the $La_{0.97}Eu_{0.03}PO_4$ nanocrystal for the band with a maximum at 613 nm is shown in Fig. 1. It is evident that the spectrum covers the wavelength range of 230–460 nm and has several maxima: at 320, 360, 375, 395, 410 nm, etc. The main maximum of the excitation spectrum is in the region of ~395 nm (3.13 eV).

131, H.Javid ave, AZ-1143, Baku
Institute of Physics
E-mail: jophphysics@gmail.com

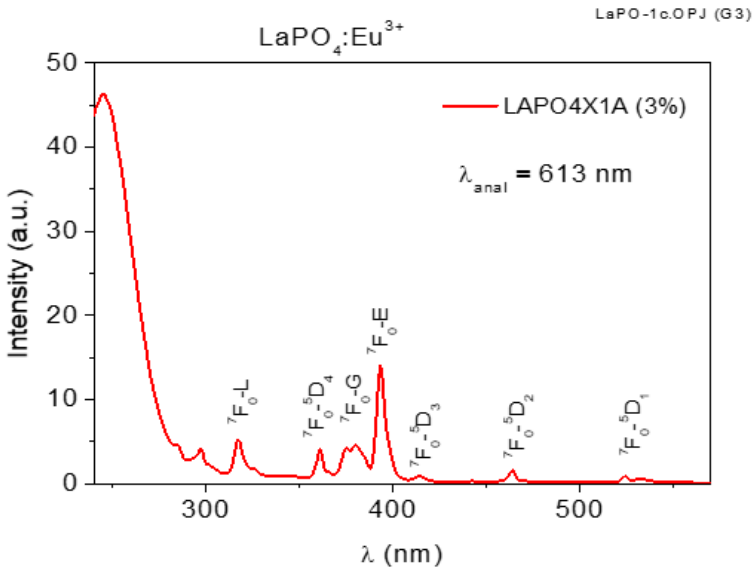


*Fig. 1.* Excitation spectrum of the $LaPO_4:Eu^{3+}$ nanocrystal.

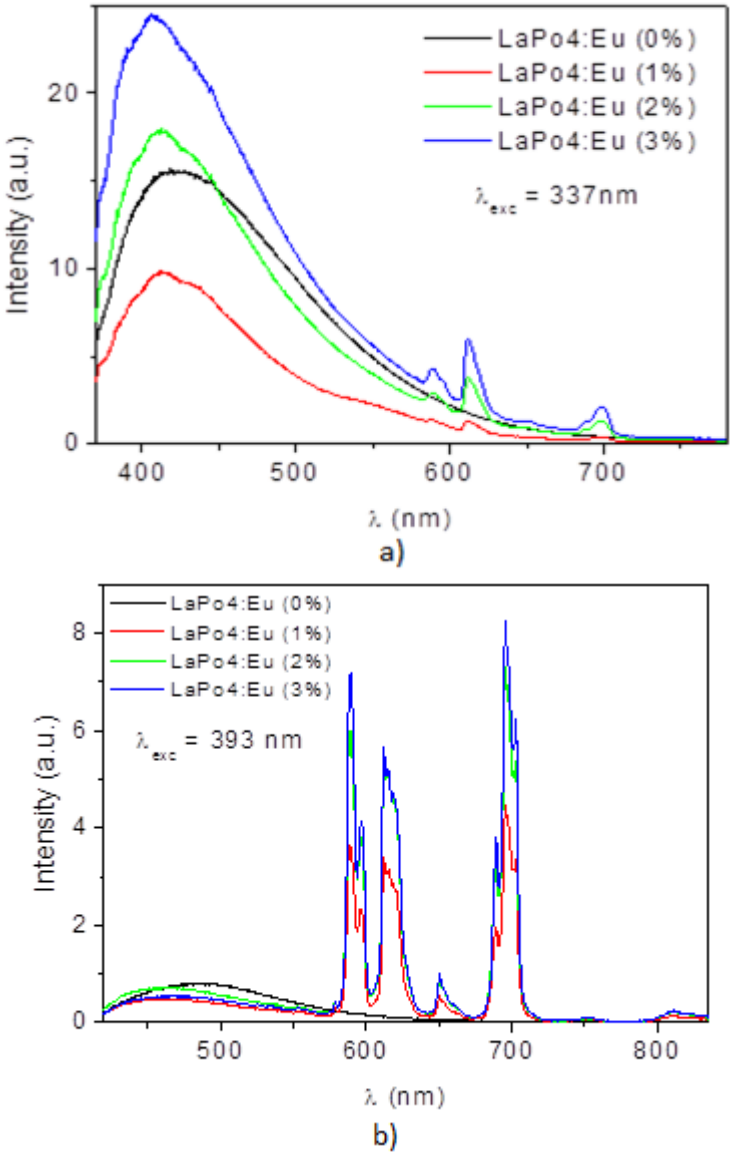


*Fig. 2.* Luminescence spectrum of the $LaPO_4:Eu^{3+}$ nanocrystal at $\lambda_{ex}$=337 nm: a - matrix radiation, b - luminescence spectrum of the $Eu^{3+}$ ion in the $LaPO_4:Eu^{3+}$ crystal.

Figure 1. shows the luminescence spectra of the $LaPO_4$ nanocrystal for various $Eu^{3+}$ concentrations (0, 1, 2, 3%) under conditions of nitrogen laser excitation ($\lambda_{ex}$=337 nm) (Fig. 2a) and at a wavelength of 393 nm (Fig. 2b). It evident that the spectrum consists of one intense broad band with emission maxima at 410 nm and a narrow line in the wavelength range of 580–710 nm. This broad band is associated with matrices, and narrow lines are associated with $Eu^{3+}$ ions (Fig. 2b).

These narrow-band emissions, which are observed in the spectra in the wavelength range 580-600nm, 610-630nm, 650-660nm and 680-710nm, are associated, respectively, with the transitions $^5D_0 \rightarrow {}^7F_1$, $^5D_0 \rightarrow {}^7F_2$, $^5D_0 \rightarrow {}^7F_3$ and $^5D_0 \rightarrow {}^7F_4$ of the $Eu^{3+}$ ion (Fig. 3). The emission intensity increases with the concentration of $Eu^{3+}$ ions and it is maximum at 3 at. %.

The emission decay kinetics for the maximum at 590nm ($^5D_0 \rightarrow {}^7F_1$) at room temperature is shown in Fig.4. Analysis of the obtained results shows that at short times ($t<5x10^{-8}$s) the intensity of photoluminescence (PL) rapidly decreases with time. In this case, the time dependence of the PL intensity for $LaPO_4:Eu^{3+}$ is exponential ($I=I_0e^{-t/\tau}$). We determine the lifetime of electrons in the trap with two values - 3ns and 14ns. In [10], a value of 42 ms was found for this decay.

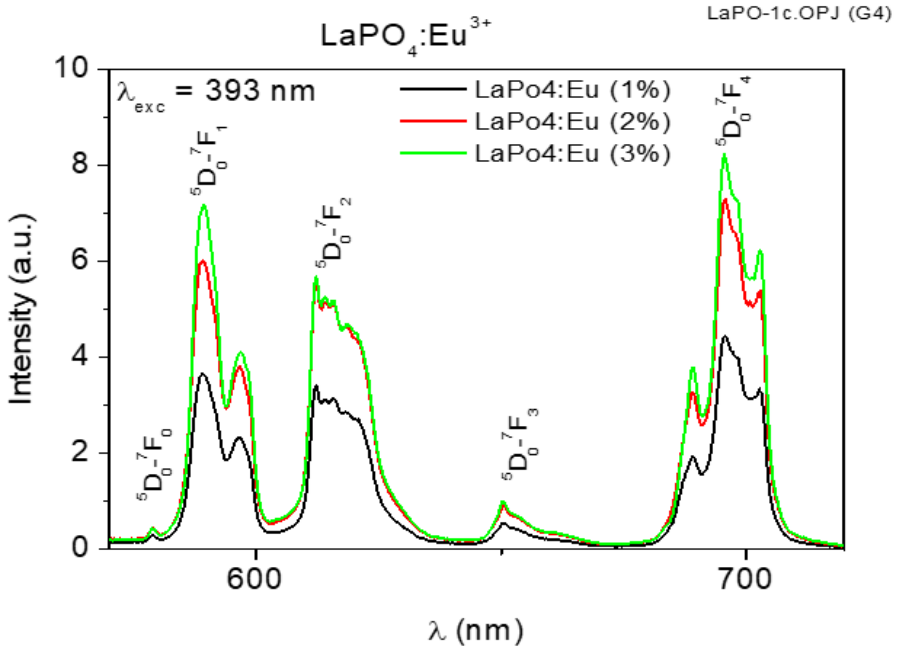


*Fig. 3.* Luminescence spectrum of the $LaPO_4:Eu^{3+}$ nanocrystal at $\lambda_{ex}$=393nm.

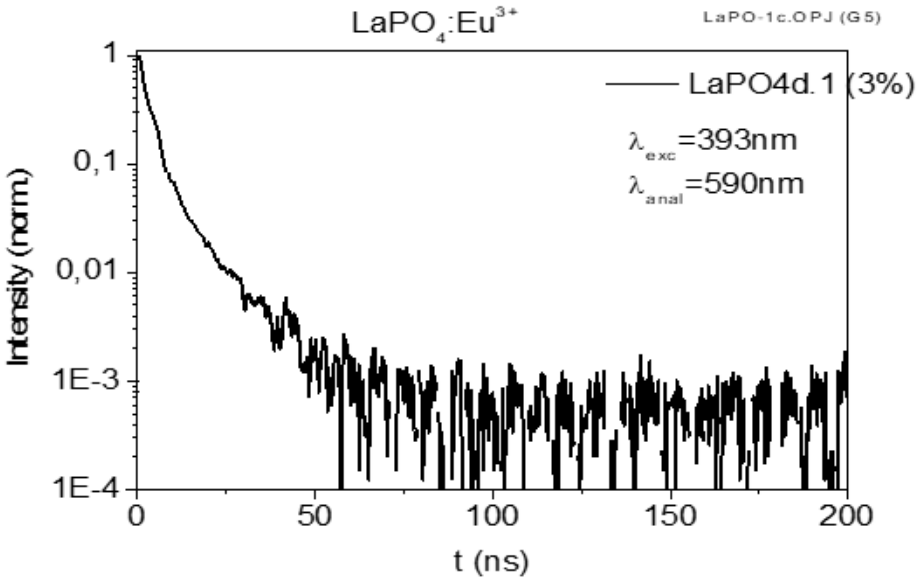


*Fig. 4.* Time dependence of the emission line of $Eu^{3+}$ ions at 590 nm in a $LaPO_4:Eu^{3+}$ nanocrystal exposed to the 393nm line.

## 4. CONCLUSION

PL measurements for $Eu^{3+}$ doped $LaPO_4$ were performed at room temperature. It was determined the PL excitation spectra under 337 nm wavelength consist of several narrow peaks due to electronic transition of $Eu^{3+}$ ions and one intense wide band is due to $LaPO_4$ matrix. The main maximum of the excitation spectrum is in the region of ~395 nm (3.13 eV) which corresponds to F-D transition of $Eu^{3+}$ ions. PL emission peaks at 337 nm and 393 nm are observed in the visible range of spectrum. The PL spectra consist of one intense broad band with emission maxima at 410 nm and a narrow line in the wavelength range of 580–710 nm. The broad band is associated with matrices, and narrow PL peaks, in the range 580-600nm, 610-630nm, 650-660nm and 680-710nm, are associated, respectively, with the transitions $^5D_0 \rightarrow {}^7F_1$, $^5D_0 \rightarrow {}^7F_2$, $^5D_0 \rightarrow {}^7F_3$ and $^5D_0 \rightarrow {}^7F_4$ of the $Eu^{3+}$ ion. The maximum emission intensity is observed at 3 at% doped $Eu^{3+}$ ions. It was determined that the lifetime of electrons in the trap with two values - 3 ns and 14 ns.


[1] *B.G. Tagiyev, O.B. Tagiyev, A.I. Mammadov, V.X. Quang, T.G. Naghiyev, S.H. Jabarov, M.S. Leonenya, G.P. Yablonskii, N.T. Dang.* Physica B: Condensed Matter 478 (2015) 58-62.

[2] *M.S. Leanenia, E.V. Lutsenko, N.V. Rzheutskij, V.N. Pavlovskii, G.P. Yablonskii, T.G. Nagiev, B.G. Tagiev, S.A. Abushev, O.B. Tagiev.* Journal of Applied Spectroscopy 82 (2) (2015) 248-253.

[3] *M.S. Leanenia, E.V. Lutsenko, M.V. Rzheutski, G.P. Yablonskii, T.G. Naghiyev, H.B. Ganbarova, O.B. Tagiev*. Optical Materials 54 (2016) 45-49.

[4] *D.T. Khan, N.T. Dang, S.H. Jabarov, T.G. Naghiyev, R.M. Rzayev, T.Q. Nguyen, H.V. Tuyen, N.T. Thanh, L.V.T. Son.* Materials Research Express 7(1) (2020) 016507.

[5] *B.G. Tagiev, O.B. Tagiev, T.G. Nagiev, S.G. Asadullaeva, M.S. Leonenya, G.P. Yablonskii, S.A. Abushov.* Optics and Spectroscopy 118(3) (2015) 389-392.

[6] *A.Sh. Abdinov, R.F. Babaeva, R.M. Rzaev, S.I. Amirova*. Inorganic Materials 48(6) (2012) 559-562.

[7] *A.Sh. Abdinov, S.A. Allakhverdiev, R.F. Babaeva, R.M. Rzaev.* Inorganic Materials 45(7) (2009) 723-727.

[8] *M.S. Leanenia, E.V. Lutsenko, M.V. Rzheutski, G.P. Yablonskii, T.G. Naghiyev, O.B. Tagiev.* Journal of Applied Physics 129(24) (2021) 243104.

[9] *S.G. Asadullayeva, Z.A. Jahangirli, T.G. Naghiyev, D.A. Mammadov.* Physica Status Solidi B 258(8) (2021) 2100101.

[10] *A.Sh. Abdinov, R.F. Babayeva, S.I. Amirova, R.M. Rzayev.* Semiconductors 47(8) (2013) 1013-1017.

[11] *A.Sh. Abdinov, R.F. Babaeva, A.T. Bagirova, R.M. Rzaev.* Inorganic materials 42(9) (2006) 937-941.

[12] *R.S. Madatov , F.G. Asadov, E.G.Asadov, T.G.Naghiyev.* Journal of the Korean Physical Society 74(5) (2019) 508-511.

[13] *R.S. Madatov, A.S. Alekperov, N.N. Gadzhieva, F.G. Asadov, Sh.A. Allahverdiev, E.G.Asadov, T.G.Naghiyev*. International Journal of Modern Physics B 33(9) (2019) 1950066.

[14] *I.A. Bondar, N.V. Vinogradova, L.N. Demyanets* and other compounds of rare earth elements: silicates, germanates, phosphates, arsenates, vanadates. M.: Nauka, 1983, 288s.

[15] *V.N. Yaglov*. Chemistry and thermodynamics of orthophosphate hydrates. Abstract doc. dis. Minsk: BTI, 1980.40s.


*Received: 18.03.2024*

# LOW VOLTAGE SEMICONDUCTOR STABILITRON

**G.S. HAJIYEVA, N.N. ABDULZADE, F.A. KAZIMOVA**
*Institute of Physics Ministry of Science and Education of Azerbaijan, AZ 1143, Baku, G. Javid Ave., 131*
kazimova-f@mail.ru

A device has been manufactured having an active region consisting of a semiconductor alloy composed of silver selenide and silver telluride taken in an equimolar ratio with an n-type conductivity. It has been determined that the proposed device is capable of stabilizing and limiting low alternating voltage. A mechanism for the observed breakdown has been suggested.

**Keywords:** stabilitron, threshold voltage, breakdown, active region.
**PACS:** 621.382.2

## INTRODUCTION

The accelerated development of semiconductor technology sets new challenges for researchers related both to the search for opportunities to create a variety of devices and to improve the electrophysical properties of the materials used in them. To date, MSM, MDM, MDS (M – metal, S – semiconductor, D – dielectric) and other more complex structures based on a range of dielectric and semiconductor materials have been investigated quite well at our Institute of Physics and the results obtained have been used in the manufacture of various devices. Similar work has also been carried out by us using binary or ternary silver chalcogenides as semiconductors and various oxides as dielectrics in the above structures, some of which [1-10] have reported the obtaining of simple experimental devices such as switching and valve elements, an air pressure sensing switch, negistors, varistors, etc.

The purpose of the presented work is to produce a stabilitron based on binary silver chalcogenides stabilizing low alternating voltages.

## EXPERIMENTAL PART, RESULTS AND DISCUSSION

Known semiconductor stabilitrons, especially today's popular silicon ones, operate in the region of p-n junction breakdown at reverse voltage and can only stabilize constant or unipolar voltage due to the asymmetry of their current-voltage characteristics (CVC). However, in order to obtain a symmetrical stabilitron characteristic, it is necessary to connect two identical stabilitrons back to back, which makes their construction much more complicated. Additionally, such stabilitrons cannot be used to stabilize small (in the order of 1.0 – 1.5 V) voltages, since they have a threshold voltage of at least 5V. Another disadvantage is that overcurrent is unacceptable in them, as it leads to the destruction of the p-n junction. We can also point to another stabilitron with a threshold voltage of 5-20 V, with an active region consisting of polycrystalline and monocrystalline silicon layers. And in this case, the need to grow a single crystal of silicon also complicates the design of the device.

Based on the above-mentioned disadvantages of operating silicon stabilitrons, and in order to achieve the objective, we have manufactured a device in the form of an MSM structure (Fig.1), the active region (1) of which is made of a homogeneous polycrystalline quasi-binary alloy of silver selenide and silver telluride with n-type conductivity ($Ag_2Se$ and $Ag_2Te$), synthesized both from initial compounds and from individual elements taken in stoichiometric ratio.

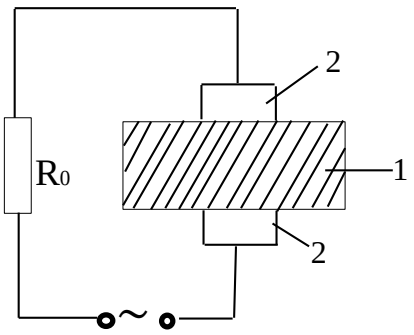


*Fig. 1.* Schematic representation of the sample structure: 1 - active area; 2 – electrodes.

Subsequently, from the alloy obtained with a concentration of $10^{18}$ -$10^{19}$ $cm^{-3}$ determined from Hall measurements, a disc of about 1.0 - 1.5 mm thickness was cut and placed between tungsten or molybdenum electrodes (2), which can be either pressed or sputtered. The resistance $R_0$ not only limits the current in the device circuit, but also plays an essential role in obtaining a stabilizing effect. So, if $R_0 = 0$, then the stabilization coefficient $k = R_s/ R_d=1$, i.e. there is no stabilization ($R_s=U/I$ – static resistance, $R_d=dU/dI$ – dynamic resistance).

The proposed device works as follows: when a voltage of any polarity is applied to it, first it is in a high-resistance state, then when the voltage reaches about 1.0-1.2 V, there is a sharp, almost abrupt transition to a low-resistance state and the CVC becomes vertical, parallel to the current axis, as can be seen from Fig. 2, which depicts the observed characteristic taken from the screen of a transistor characteristics monitoring device (TCMD) type curve



131, H.Javid ave, AZ-1143, Baku
Institute of Physics
E-mail: jophphysics@gmail.com

tracer (a) and in static mode (b). The threshold voltage (1.0 -1.2 V) remains constant when the stabilization current is varying from 5-10 mA to 250-300 mA.

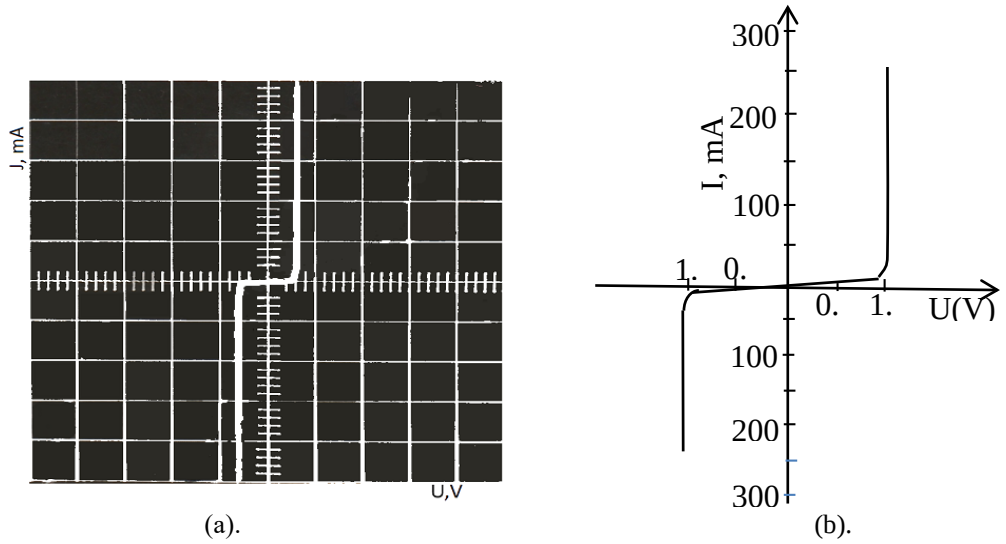


(a). (b).

*Fig. 2.* CVC of the device, taken at 300K: a) from the curve tracer screen; b) in static mode; horizontal scale 2 V/div., vertical - 50 mA/div.

The CVC of the device depends neither on the method of creating the electrodes nor on their arrangement, which does not limit the structural design of the device. In addition, it is easy to fabricate as the active region is single-layer and no p-n junction or single crystal growth is needed.

In dependence on the nature of the physical processes that cause a sharp increase in current, thermal, avalanche and tunneling breakdowns are distinguished.

The breakdown observed by us is not thermal, since it is characterized by the presence of a negative resistance region in the working section of the CVC (Fig. 3, curve 1) [11]. Avalanche breakdown, usually caused by impact ionization of the semiconductor, is also excluded, since it occurs at sufficiently high electric field strength ($10^5$ - $10^6$ V/cm and more) (section 2 of the characteristic).

We believe that at a given small threshold voltage (1.0 -1.2V), an electric field may arise that is sufficient to directly transfer electrons from the electrodes to the semiconductor or to cause intense leakage of electrons from one electrode to another through the active region, leading to tunnel breakdown (section 3 of the CVC).

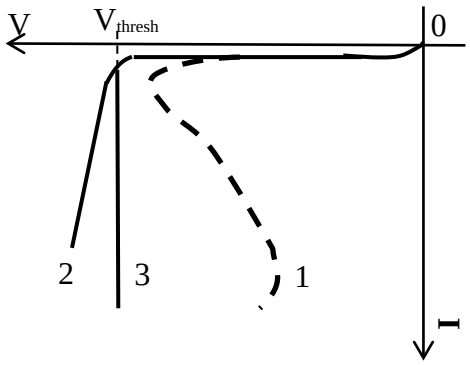


*Fig. 3.* The character of current growth at different types of breakdown: 1- thermal, 2- avalanche, 3-tunnel.

## CONCLUSION

Compared to known stabilitrons, proposed by us device provides the ability to stabilize and limit small alternating voltages, as well as can be used as a two-way limiter, two-way rectangular pulse shaper, electric key, etc.

[1] *Ш.М. Алекперова, Г.С. Гаджиева, И.А. Ахмедов, Р.Г. Ахмедзаде*. II Респуб. конф. " Актуальные проблемы физики" БГУ, 2003, стр.13.

[2] *Ш.М. Алекперова, Г.С. Гаджиева, Н.Н. Абдулзаде, И.А. Ахмедов, Р.Г. Ахмедзаде*. Труды III Между. научно - техн. конф. “Микроэлектронные преобразователи и приборы на их основе” Баку-Сумгаит, МЭПП, 2003, с.44.

[3] *Ш.М. Алекперова, Г.С. Гаджиева, Н.Н. Абдулзаде, И.А. Ахмедов, Р.Г. Ахмедзаде, М.И. Агаев.* Сборник материалов, Междун. конф. посвященной 85 - летию Г.Б. Абдуллаева. Баку, 2003, стр.

[4] *Ш.М. Алекперова, Г.С. Гаджиева, И.А. Ахмедов.* Известия НАН Азерб. Баку. 2005, т. XXV, № 5, стр.123-128.

[5] *Ш.М. Алекперова, Г.С. Гаджиева, И.А. Ахмедов.* Междунар. конф. Физика – 2005, № 228, стр. 863 – 865.

[6] *Ш.М. Алекперова, Г.С. Гаджиева, И.А. Ахмедов, Л.Н. Алиева.* Известия НАН Азерб. Баку. 2006, т. XXVI, № 5, стр.153 - 159.

[7] *Ш.М. Алекперова, Г.С. Гаджиева, Х.Д. Джалилова, И.А. Ахмедов.* Межд. конф., посвященная 100 – летию академика Х.И. Амирханова “Физика 1-2 “, 2007, т. XIII, стр. 258 – 259.

[8] *Г.С. Гаджиева, И.А. Ахмедов, Н.Н. Абдулзаде.* Инженерно – физич. журнал, Минск, АН Беларуси 2013, т. 86, № 2, стр. 447 – 450.

[9] *Г.С. Гаджиева, И.А .Ахмедов, Н.Н. Абдулзаде.* Инженерно – физич. журнал. Минск АН Беларуси, 2015, т. 88, № 4, стр. 994 -997.

[10] *Г.С. Гаджиева, Ф.А. Казымова, Т.Ш. Ибрагимова, К.О. Тагиев, Э.Г. Асадов.* International Conference: modern trends in physics. Baku – 2017, p. 421 -423.

[11] *Г.И. Епифанов.* Физика твердого тела. Москва, изд.-во «Высшая школа» 1977, с.288.

*Received: 18.03.2024*

# SCALING PROPERTIES OF DIRAC MATRICES, THE GRAVIATIONAL FIELD, AND CONSISTENTLY LIFE LIKE TRANSFORMATION LAW BEHAVIOR ASPECT OF THESE MATRICES. DIRAC MATRICES AND DARK MATTER

**F.A. MAMEDOV**
*Institute for Physical Problems, Baku State University, Azerbaijan*
*e-mail: mail.quanta02@gmail.com, phone: (994) 12 510 18 22*

Dirac matrices reveal the certain scaling property in all three known representations. One can associate this scaling property with the basic ingredients of life as a result of its thorough analysis. Different aspects of the Dirac equation and Dirac matrices on the Lorentz transformations are analyzed to get a clearer picture on this circumstance. Signs of the dark matter and Dirac matrices relations are also discussed.

**Keywords**: Scaling properties of the Dirac matrices, boson mass - coupling constant relation, angular momentum, magnetic moment, Dirac equation, life like transformation laws of the Dirac matrices, Mayorana equation, dark matter.
**PACS:** Electroweak interactions, in unified field theories, 12.10.Dm

The original goal of this work was an attempt to connect the basic ingredients of quantum field theory to the domain of Riemannian Geometry and and get clearer interpretation of the formula

$$M_W / M_B = g/gN \qquad (1)$$

extensively discussed in the previous works ([4] and [6]). This way one could also get a strong bridge between quantum field theory and A. Einstein's theory of gravity. One might tend to think that with some minor adjustment of the Riemannian Geometry on quantum fluctuations it would encompass all the possible theories of physics. This partial derivatives based theory describes all the possible patterns in space - time. However, as discussed further in this work, Dirac equation has a wider scope in several aspects than Lorentz invariance friendly only Riemannian Geometry. Dirac equation can be regarded as a complex relation between the partial derivatives of the wave function and mass after the shift in the symmetry occurs and mass of fermions appears. Local gauge transformations, that is presence of space - time, necessitate the replacement of Lie derivatives by the covariant derivatives:

$$M_: \to M_: + i(gN/2)\, B_: \qquad (2)$$

for the $B_:$ field for example. Eq.(1) is consistent with this view of appearance of space - time, the appearance of space - time, that is generation of masses of particles is indispensably connected with the presence of the coupling constants and vice versa. This view of formation of space - time is certainly incompatible with the possibility of existence of the scalar fields. In the case of complex scalar fields the charge, the conserved quantity exists even for the global gauge transformations which do not require the presence of space - time. Dirac equation must have a broader scope than equations of the gravitational field, its Lorentz invariance ingredient can be regarded as a consequence of the dotted quantities' independence of the space - times formation and expansion of the universe. Derivative free charge density for the wave function of Dirac equation $/\Theta(_:\Theta$ also tells us about this nature of this equation. It is unlikely that one can get a Lorentz covariant form of Dirac equation (that is how A. Einstein wanted to see the fundamental equations of physics) in the form

$$iM_:\Theta(x) - m(N_:\Theta(x) = 0 \qquad (3)$$

which would make the statement above weaker. Here $(N_:$ is some modified form of the $(_:$ matrix. That way Dirac equation would be covariant similar to the A. Einstein's gravitational field equation:

$$R_{:<} - (1/2)g_{:<}R = -kT_{:<} \qquad (4)$$

From the other side it is not a single - particle nature for the massive fermions, the necessity of the existence of the electron - positron pair as its full set of solutions, particles and the distance between them, means the existence of space - time. Lorentz transformation of the Dirac equation dwindles down to changing the 'orientation' of the Dirac spinor only (see the importance of the angular momentum in this context in the further discussions):

$$(i/M - m)\Theta(x) = 0 \;6\; 7_{1/2}[i/M - m]\Theta(7^{-1}x) = 0 \qquad (5)$$

Here 7 and $7_{1/2}$ are four -dimensional and Dirac spinors representations of the Lorentz transformations, respectively.

Could the Lorentz transformation property of the Dirac matrices be the first clue how quantum fields are connected to the life activity of the living creatures? There are a number of features of these matrices consistent with this guess. Lorentz transformations of the spinor indices of Dirac matrices is equal to their vector indices'
Lorentz transformations:

$$7_{1/2}(_:7_{1/2} = 7^{<}{}_:(_< \qquad (6)$$

The spinor indices, the elements of the Dirac matrices relate to their inner part, meanwhile vector transformations regard every Dirac matrix as whole,

131, H.Javid ave, AZ-1143, Baku
Institute of Physics
E-mail: jophphysics@gmail.com

indivisible unit. One can say that Eq.(6) describes the inner activity of the living creature and its movement in the space at the most basic level. One can formulate this thought in the following, slightly different form too. Lorentz transformations on the inner part of Dirac matrices, live matter generator is equal to their Lorentz transformation as a vector: Dirac equation is a bridge between the live matter generating structure (with Heisenberg's uncertainty principle) and Lorentz invariant world (space - time). Dirac equation based probability density's space - time independence is also consistent with this conclusion, Dirac equation and life activity have a larger scope than just this particular universe.

It should be obvious that life is not some peculiar small fluctuation in the galactic processes. The shift in the symmetry process's eventual destination must be the formation of life the way we know it. The certain interesting features of the nuclear binding energies and their relation to the human life activity discussed in [4] could be specific for our universe. In other words, the life must have a broader range of representations, not just the one manifesting itself in our universe: better understanding the connection between the basic elements of life and quantum field theory could help in building the so called 'theory of everything' for our universe. So S. Weinberg's dream to see the consciousness process in the equations of quantum field theory is unachievable in the current state of the theory. In other words, in order to bring physics to the level encompassing human psychology we have to have the theory of the universes. Possibly paraphrased words of S. Weinberg: through the final theory to see why the world is this way but not another way.

Eq.(6) already tells us that the well - known elements of the Dirac matrices are not simply numbers or coefficients, they are elements of the certain tensor similar to the Ricci tensor $R_{:<}$ or the metric tensor $g_{:<}$ in th local coordinate system of the electron - positron system (see [8]). Shifting the quantum field theory calculations from the local coordinate system of particles, from the Dirac matrices coordinate system to the certain general coordinate system might noticeably simplify these calculations. This general coordinate system could also mean the usage of the Heisenberg's uncertainty principle to the greater extent. It is interesting that twelve out of sixteen elements of each of these matrices are zeros, 3/4 of them, this is approximately how much the current science ascribes to the dark matter in the galactic processes (by taking into account that the values of these matrix elements should not be necessarily distributed uniformly). Dark matter in the galaxies also reveal their own scaling property [9]. Mayorana equation can also be considered just a Dirac equation with non unit mass matrix M in this context:

$$i\,/M\Theta(x) - m\Theta_C(x) = 0\ 6\ i\,/M\Theta(x) - M\Theta_C(x) = 0 \quad (7)$$

There is another aspect of the Dirac matrices which also supports the idea that they describe the building block of life generation. Angular momentum has a Heisenberg's uncertainty principle in a self - contained form, meanwhile Dirac equation produces the correct value for the electron's magnetic moment which is indispensably connected to its angular momentum. The core of the live matter or the living creature is inseparable into parts system and it is essentially self - contained system, the $(_3$ matrix corresponding to the direction of the certain value of the angular momentum (and spin for that matter) does not scale down into smaller similar units in all three representations of Dirac matrices. Shift in symmetry process utilizing Eq. (1) also occurs in a self - consistent way, without referring to another extra field [4]. Here it is also worth mentioning that angular momentum commutation relations are also in a self - contained form with no 'break - down' and incorporates all three components of angular momentum:

$$[L_x, L_y] = i\Sigma L_z \text{ etc.},$$

The commutator of the one - dimensional position and momentum operators does not include these quantities:

$$[x, p_x] = i\Sigma$$

The difference of the order of taking measurements leaves a stable residue of the order of quantum fluctuations. A certain core property of life could well be of this nature, however different from the special relativity style measurements, matrix mechanics does not incorporate time difference of these measurements and it is hard to assess this feature of quantum mechanics on the ongoing discussion.

Dirac spinors related representation of the Lorentz transformations is essentially a commutator of the $(_:$ matrices. The connection of this representation $S_{:<}$ to the space - time representation of the Lorentz transformations is achieved only by an (additional) commutation relation of $S_{:<}$ with the $(_:$:

$$[(_:, S_{\forall\exists}] = (J_{\forall\exists})_:^{<}\,(_< \quad (8)$$

Here $(J_{\forall\exists})_:^{<}$ is a four - dimensional space - time representation of the Lorentz transformations. This aspect of the Dirac matrices $(_:$ also tells that Dirac equation has a larger scope than four - dimensional space - time. With massless fermions the Dirac equation breaks down into Weyl equations, so fermions getting massive as a result of the shift in the symmetry is also among the initial conditions necessary for the formation of life processes (to have Dirac matrices based actvities present with the matrices' above mentioned features).

Particle masses enter the Lagrangian through covariant derivatives (see Eq.(1)), gauge invariant way, and through mass mass terms which violate gauge invariance. The former has a more complex structure and the latter is the essence of building the space - time around us. Meanwhile both the wave function and its covariant derivative transform the same way under the gauge transformations.

The superposition of states feature of quantum

mechanics should also be one of the necessary conditions for the existence of life activity. Where do all the living creatures get the capacity of decision making from? At base level this capacity could just be choosing some combination of states from the system of states by the living creature influenced by the certain external field, wind. This aspect of living creatures also supports the quantum mechanical - quantum field theory origin hypothesis of life on the Earth.

## CONCLUSIONS

The Dirac equation is a bridge between Lorentz invariant world and quantum mechanics world governed by the Heisenberg uncertainty principle. Analysis of the Dirac matrices from the different perspectives consistently point to their certain feature, which one can readily associate with the basic ingredients of life. Signs of the dark matter can also be seen in the elements of the generalized Dirac matrices with this approach to the Dirac equation.

## ACKNOWLEDGEMENTS

The author would like to thank Sadiyar Rahimov, director of the Institute for the Physical Problems, Baku State University, for the several helpful discussions of the mass scaling relations throughout the galaxies in the universe.

---

[1] *S.L. Glashow.* Nuclear Physics 22 (1961), 579
[2] *S. Weinberg.* Physical Review Letters, 19, 1264
[3] *A. Salam, N. Svartholm.* Proceedings of the Eighth Nobel Symposium, Almqvist \& Wiksell, Stockholm (1968)
[4] *F. Mamedov,* hep-ph/0606255
[5] *F. Mamedov,* hep-ph/0607010
[6] *F.A. Mamedov,* SU(2)L x SU(2)R symmetry of the fermions and the vector bosons, the fermionic origin of the local gauge transformations, the visible traces of the flickering nature of the early stages of the universe's formation, AJP Fizika C, 2023.
[7] *S. Eidelman et al.,* Phys. Lett. B 592, 1 (2004)
[8] *Sam Walters,* How Eintstein Got His Field Equations, arxiv.org/abs/1608.05752
[9] *P. Salucci, A. Burkert,* Dark Matter Scaling Relations, *arXiv:astro-ph/0004397*
[10] Collaboration, CMS (2019). "Evidence for light-by-light scattering and searches for axion-like particles in ultraperipheral PbPb collisions at /sNN = 5.02 TeV". Phys. Lett. B. 797: 134826. arXiv:1810.04602. doi:10.1016/j.physletb.2019.134826. S2CID 201698459
[11] *R.W. Brown, K.L. Kowalski and S.J. Brodsky.* Phys. Rev. D, 28:624, 1983.
[12] https://www.admin.ch/gov/en/start/documentation/media-releases.msg-id-82143.html
[13] http://fafnir.phyast.pitt.edu/particles/sizes-3.html
[14] http://nscl.msu.edu/news/news - 25.html

*Received: 27.03.2024*

**ISSN 1028-8546**
**2024, Vol. XXX, №1**
**Section: E**

# *CONTENTS*